

MECHANICAL BEHAVIOR OF METALLIC FOAMS

L. J. Gibson

Department of Materials Science and Engineering, Massachusetts Institute of Technology, Cambridge, Massachusetts 02139; e-mail: ljgibson@mit.edu

Key Words cellular solids, microstructure, properties, moduli, strength

■ **Abstract** Metallic foams have a combination of properties that make them attractive for a number of engineering applications, including lightweight structural sandwich panels, energy absorption devices, and heat sinks. For many potential applications an understanding of the mechanical behavior of these foams is essential. Recently, there has been substantial progress in identifying the mechanisms of deformation and failure in metallic foams. Here, we summarize the current understanding of the elastic moduli, uniaxial strength, yield criterion, creep, and fatigue of metallic foams.

INTRODUCTION

Metallic foams can be made by a number of novel processes. Although aluminum foams are the most common, nickel, copper, zinc, and steel foams are also available. Micrographs of four closed-cell and one open-cell aluminum foams are shown in Figure 1.

Metallic foams have a combination of properties that make them attractive in a number of engineering applications. In structural sandwich panels, they offer lower weight than conventional honeycomb or stringer-stiffened designs for some, although not all, loading configurations. Recently developed processing techniques allow the manufacture of panels of complex shape with integrally bonded faces at relatively low cost. The capacity of metal foams to undergo large strains (up to about 60–70%) at almost constant stress allows significant energy absorption without generating damaging peak stresses, thus making them ideal for energy absorption devices. Open-cell metallic foams make excellent heat dissipation devices due to their high thermal conductivity, their high internal surface area, and the connectivity of the voids, which allows a cooling gas to pass through.

The literature on metallic foams is growing. The book *Cellular Solids* by Gibson & Ashby (1) provides a broad survey of the understanding of the mechanical behavior of a wide range of cellular solids. *Metal Foams: A Design Guide* summarizes the results of recent research in a format accessible to the design engineer (2). The patent literature, as well as reviews by Banhart & Baumeister (3) and Davies & Zhen (4) describe the processing of metal foams. The potential use of metallic

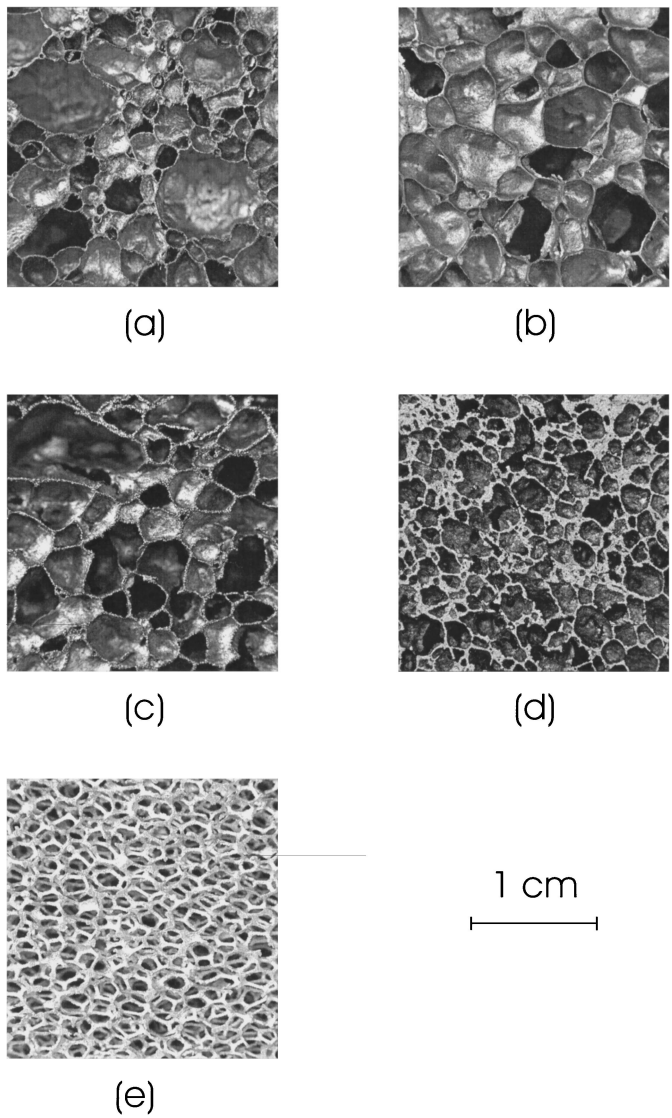


Figure 1 Micrographs of metallic foams. (a) Alcan, (b) Alporas, (c) Alulight, (d) Fraunhofer, (e) ERG Duocel (reproduced from 22, with permission of Elsevier Science).

foams in structural sandwich panels, energy absorption devices, and heat sinks is evaluated in the review article by Evans et al (5). Journal articles on metallic foams appear regularly in *Acta Materialia*, *Materials Science and Engineering A*, the *International Journal of Mechanical Sciences*, and in *The Journal of the Mechanics and Physics of Solids*.

This article reviews the mechanical behavior of metallic foams. Processes for making metallic foams and the microstructural features relevant to mechanical behavior are briefly discussed. The results of micromechanical models for the moduli and strength of open- and closed-cell foams are presented and compared with data for metallic foams. The effect of imperfections, such as curved cell walls, is discussed. Size effects can be important in metallic foams, due to the relatively large cells (on the order of a few millimeters). Models for the effect of the ratio of specimen size to the cell size on the uniaxial and shear properties of foams are summarized and compared with data. Phenomenological yield criteria giving the multiaxial stress states required for failure are presented. Finally, the high-temperature creep and cyclic fatigue behaviors are described.

PROCESSING

Metal foams have been made for over 40 years. Today, they are made using melt processing, powder processing, or vapor deposition techniques. A list of suppliers is available in *Metal Foams: A Design Guide* (2). Methods are also available for making porous metals with relative densities greater than those of foams (i.e. greater than about 0.3).

Melt Processing Routes

One of the first techniques developed for making metallic foams was to decompose metal hydride particles to evolve hydrogen gas in a molten alloy (4, 6, 7). Typically titanium hydride, TiH_2 , is used as the blowing agent in an aluminum alloy, although other hydrides and alloys can be used. Initial production was limited by inhomogeneities in cell structure and density that resulted from the non-uniform distribution of hydride throughout the melt. Improved hydride distribution can be achieved through high-speed mixing and the formation of an oxide layer on the hydride powder, allowing better control of the hydride decomposition kinetics (4, 8, 9). Smaller, more uniform cell size can be achieved through the introduction of viscosity-enhancing additives to the melt (4, 10). The commercial aluminum foam, Alporas (Shinko Wire, Amagasaki, Japan), uses calcium as the viscosity-enhancing additive and titanium hydride as the blowing agent.

Aluminum foams can also be made by adding silicon carbide, aluminum oxide, or magnesium oxide particles into molten aluminum and blowing a gas (air, nitrogen, or argon) into the mix using rotating impellers to produce and distribute fine bubbles. The molten foam is then pulled onto a conveyor belt for cooling. This

process was developed by Alcan (11) and Norsk Hydro (12). Foams produced this way are commercially available from Cymat (Mississauga, Ontario, Canada).

Open-cell metallic foams can be made by investment casting (4, 13). An open-cell polymer foam is coated with a slurry of heat-resistant material (e.g. a mixture of mullite, phenolic resin, and calcium carbonate). After drying, the polymer is driven off by heating and molten metal is cast into the mold, giving a replica of the initial polymer foam structure. The mold material is then removed by a pressurized water jet. Although aluminum alloys are most commonly used, other metals can also be made into foams this way. The commercial product Duocel (ERG, Oakland California) is made using this technique.

Powder Processing Routes

The most widely used powder metallurgy technique for making foams also exploits the decomposition of metal hydrides to evolve hydrogen gas. A mixture of powdered metal alloy and powdered metal hydride is compacted and formed, usually by extrusion or rolling. The formed section is then heated to temperatures above the decomposition temperature of the hydride and near the melting point of the alloy to produce the foam (13–15). Near net shape parts can be produced by heating the compacted precursor material in a hollow mold so that the foam expands to the shape of the mold. More complexly shaped parts can be made by injecting the foam while it is still expanding into appropriate molds. Sandwich panels with integral skins can be made by roll-cladding solid metal faces onto a core of the compacted precursor material and heating the resulting plate to expand the core. Curved sandwich panels can be produced by deformation processing of the panel before heating. The most common application of this technique is in making aluminum foams using titanium hydride, although it has also been used to make tin, zinc, lead, and brass foams. This technique is used by the Fraunhofer Institute in Bremen, Germany and by Mepura in Ranshofen, Austria (trade name Alulight[®]).

Deposition Techniques

Deposition techniques use an open-cell polymer foam as a mold (4, 13). The polymer foam is first made electrically conductive by dipping it in a graphite solution or by coating it by metal vaporization. Metal (typically copper or nickel) is then electroplated onto the foam. The initial polymer foam is subsequently burned out, leaving hollow cell edges in the metal foam.

Additional Processes for Making Porous Metals

A number of additional techniques are available for making porous metals with relative densities higher than those of true foams (i.e. greater than 0.3). In the low-density core (LDC) process developed at Boeing, a titanium alloy sandwich structure with a roughly 60–80% dense core is produced (16, 17). Metal powder is packed into a can, which is outgassed and then pressurized with argon gas.

The can is hot isostatically pressed to consolidate the metal powder fully. After consolidation, the can is rolled to form a sheet and then heated to expand the entrapped gas in the consolidated powder. The can forms the faces of the sandwich, and the expanded metal forms the core.

Hollow metal spheres, made by the reduction of hollow ceramic spheres, can be diffusion bonded to form a lightweight material (18). The ceramic spheres are made by blowing gas into a slurry by means of a coaxial nozzle. The cylindrical tube of slurry exiting the nozzle closes off as a result of surface tension to form a stream of spherical droplets that are then densified by sintering. Hollow metal spheres made of stainless steel, titanium alloy, and nickel have all been made using this process.

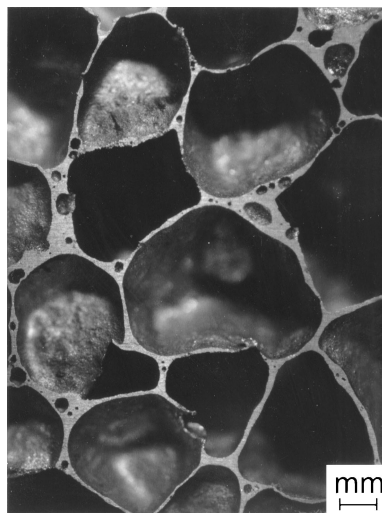
In the GASAR process, hydrogen gas is dissolved in molten metal in a pressurized furnace (19, 20). When the metal is directionally solidified, the gas comes out of solution, forming bubbles at the freezing front. Cooling the melt from the bottom produces parallel, cylindrical voids in the structure, cooling it radially produces radial pores. Integral skin sandwich construction can be produced by varying the pressure within the chamber during the solidification process. Porous copper, aluminum, iron, nickel, and titanium have all been made with this technique; the porosity that can be achieved depends on the solubility of hydrogen in the molten metal.

MICROSTRUCTURE

Micrographs of a several aluminum foams are shown in Figure 1. The microstructure is made up of an interconnected network of struts or plates that form the edges and faces of polyhedral cells. The single most important microstructural feature affecting the mechanical properties of foams is the volume fraction of solid, or relative density, the ratio of the density of the foam to that of the solid, ρ^*/ρ_s ¹. Metallic foams typically have relative densities in the range of 0.03 to 0.3. Foams are described as open- or closed-celled. Those shown in Figure 1a–d are all closed-cell, with faces separating the voids of each cell; that shown in Figure 1e is open-celled. Micromechanical models for open- and closed-celled foams are described in the next section. The cell size of most metallic foams is in the range of 2 to 10 mm (21, 22). Although the mechanical properties of foams are sensitive to the ratio of the cell wall thickness to length, most do not depend on the absolute cell size. The cell shape of metallic foams ranges from equiaxed to ellipsoidal, with the ratios of major to minor axis lengths up to 1.5 (21). The elongation of the cells corresponds to the rise of gas in the liquid (or mushy) state during processing. Foams are typically stiffer and stronger when loaded parallel to the major principal direction. Finally, the cell wall has an influence on the

¹Throughout this review, a superscript asterisk refers to a property of the foam whereas a subscript s refers to a property of the solid from which the foam is made.

Figure 2 Micrograph showing curvature of cell walls in a closed cell aluminum foam (Alporas) (reproduced from 21, with permission of Elsevier Science).



mechanical behavior of foams. The cell walls of some metallic foams are curved, possibly as a result of partial cell collapse during solidification (21–23) (Figure 2). Cell wall curvature reduces the mechanical properties below the values that would be expected if the walls were planar. The composition of the cell wall also affects the properties of the foam. The additives and foaming agents used to process metallic foams often result in unconventional alloys. For instance, in one process the use of calcium as a thickening agent and titanium hydride as a blowing agent introduces Al-Ca-Ti precipitates into the microstructure (21, 23). In this case, the yield strength of the cell wall material is measured directly using indentation techniques. Measured values for microstructural features of the aluminum foams shown in Figure 1 are summarized in Table 1.

MICROMECHANICAL MODELS FOR FOAMS

A schematic stress-strain curve for a foam in uniaxial compression is shown in Figure 3. Initial linear elasticity is followed by a roughly constant stress plateau that continues up to large strains beyond which the stress increases sharply. Previous studies of polymer foams have found that the linear elastic response is related to cell edge bending in open-cell foams and to the edge bending and face stretching in closed-cell foams (1, 24–30). As the stress increases, the cells begin to collapse at a roughly constant load by elastic buckling, yielding, or fracture, depending on the nature of the cell wall material (1, 25–27, 31–37). Once all of the cells have collapsed, further deformation presses opposing cell walls against each other, increasing the stress sharply: This final regime is referred to as densification.

TABLE 1 Microstructural features of aluminum foams

Foam	Relative density, ρ^*/ρ_s (—)	Open/closed	Ratio of major/minor axis length	Cell size (mm)	Average curvature, $L/2R$ (—)	Solid modulus, E_s (GPa)	Solid yield strength, σ_{ys} (MPa)
Duocel	0.06–0.14	Open	1.1–1.8	2.5–4.5	—	69	193–200
Alcan	0.03–0.14	Closed	0.8–1.5	3.4–13.2	0.31	93	138–330
Alporas	0.07–0.09	Closed	~1	4.5	0.21	69	130–172
Alulight	0.10–0.30	Closed	~1	4.2	0.37	69	130–250
Fraunhofer	0.07–0.45	Closed	~1	2.6	—	69	250

After Andrews et al (22).

Yield strengths can vary depending on processing variables (e.g. alloys and additives).

In this section we review models for the mechanical behavior of ideal open- and closed-cell foams. The complex cell geometry of foams is difficult to model exactly. Several approaches are described in the literature. The simplest technique is to use dimensional arguments to model the mechanisms of deformation and failure (1, 27). The results give the dependence of the properties on relative density and on cell wall properties but not on cell geometry; the constants relating to cell geometry are found by fitting the model equations to experimental data. A second method is to analyze a repeating unit cell, such as a tetrakaidecahedron, using structural mechanics or finite elements (24, 26, 28, 30, 37, 38). This method gives the dependence of the properties on the geometry of the unit cell; this can be used as an estimate of the geometrical constants of the foam microstructure.

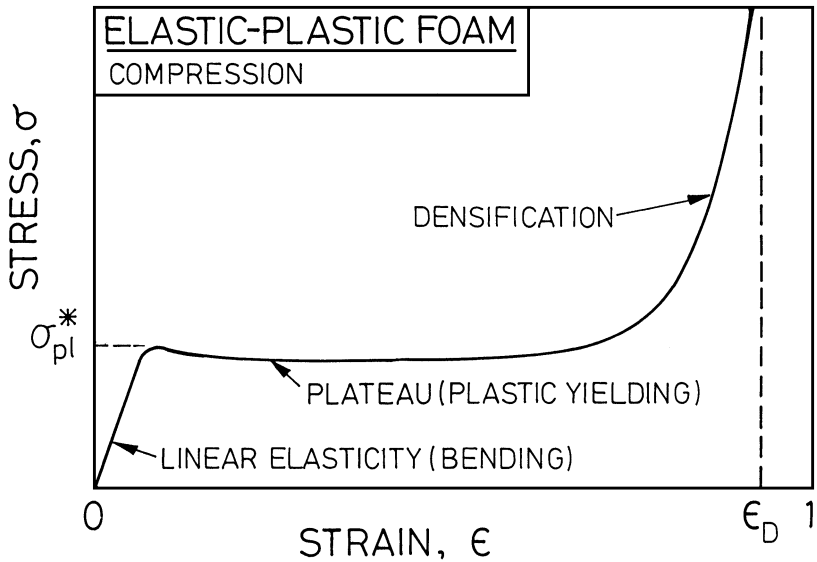


Figure 3 A schematic stress-strain curve for a foam showing the linear elastic, stress plateau and densification regimes (reproduced with permission from 1).

A third approach is to model a spatially periodic arrangement of several random Voronoi cells using finite element analysis (29). The advantage of this approach is that it gives the best representation of the cell geometry of foams, although it is computationally intensive. Here we review the use of dimensional arguments to show the way in which the properties depend on the relative density of the foam and the solid cell wall properties. We refer to the results of unit cell and finite element models to estimate the magnitude of the constants relating to the cell geometry. In the following section we describe the deformation and failure of metallic foams, modify the models to account for imperfections in their cell structure and compare the results with data for metallic foams.

In open-cell foams, the cell edges initially deform by bending. The Young's modulus can be calculated from a dimensional analysis of the edge bending deflection. The relative modulus (that of the foam, E^* , divided by that of the solid, E_s) is proportional to the square of the relative density, ρ^*/ρ_s :

$$\frac{E^*}{E_s} = C_1 \left(\frac{\rho^*}{\rho_s} \right)^2, \quad 1.$$

where C_1 is a constant related to the cell geometry. Analysis of a tetrakaidecahedral unit cell with the cell cross section defined by Plateau borders finds $C_1 = 0.98$ (30, 38). This value is confirmed by data for a wide variety of open-cell polymer foams that give $C_1 \sim 1$. In shear, the cell edges also respond by bending, so that

$$\frac{G^*}{G_s} = C_2 \left(\frac{\rho^*}{\rho_s} \right)^2, \quad 2.$$

with $C_2 \sim 3/8$. The Poisson's ratio is simply the ratio of two strains and is independent of relative density; measured values suggest that for many foams it is about $1/3$.

Closed-cell foams are more complicated. When the foam is loaded, there is stretching of the planar cell faces in addition to bending of the cell edges, adding a linear density dependence to Equation 1:

$$\frac{E^*}{E_s} = C_1 \left(\frac{\rho^*}{\rho_s} \right)^2 + C'_1 \left(\frac{\rho^*}{\rho_s} \right). \quad 3.$$

Finite element analysis of a closed cell tetrakaidecahedral unit cell and of random, Voronoi closed cells suggests that $C_1 = C'_1 \sim 0.32$ (29, 39). For low density foams, the second, face stretching, term dominates so that

$$\frac{E^*}{E_s} \approx 0.32 \left(\frac{\rho^*}{\rho_s} \right). \quad 4.$$

For isotropic closed cell foams we expect the shear modulus to be about $3/8$ of the value of the Young's modulus and the Poisson's ratio to be about $1/3$. Note that the Young's modulus corresponding to the Hashin-Shtrikman upper bounds for the bulk and shear moduli of a dense solid with voids is somewhat higher than

this: $E^*/E_s = 0.5 (\rho^*/\rho_s)$ (40, 41). A comprehensive review of the elastic moduli of ideal cellular solids is provided by Grenestedt (42).

The plateau stress for foams made from an elastic-plastic material is reached when the cells begin to collapse plastically. For open-cell foams, cell collapse corresponds to the formation of a mechanism of plastic hinges in the bent cell edges. Dimensional arguments give the plastic collapse stress, σ_{pl}^* , relative to the yield strength of the solid cell edge material, σ_{ys} as

$$\frac{\sigma_{pl}^*}{\sigma_{ys}} = C_3 \left(\frac{\rho^*}{\rho_s} \right)^{3/2}, \quad 5.$$

where the constant C_3 is related to the cell geometry. Data for a wide range of foams suggest that $C_3 \sim 0.3$.

Closed-cell foams have an additional contribution to their strength: yielding of the stretched cell faces. The stress required for this is linearly proportional to the relative density of the foam so that

$$\frac{\sigma_{pl}^*}{\sigma_{ys}} = C_3 \left(\frac{\rho^*}{\rho_s} \right)^{3/2} + C'_3 \left(\frac{\rho^*}{\rho_s} \right). \quad 6.$$

Finite element analysis of a tetrakaidecahedral unit cell with flat faces suggests that (39)

$$\frac{\sigma_{pl}^*}{\sigma_{ys}} = 0.33 \left(\frac{\rho^*}{\rho_s} \right)^2 + 0.44 \left(\frac{\rho^*}{\rho_s} \right). \quad 7.$$

For low relative densities, the second term, corresponding to axial yielding of the faces, dominates so that

$$\frac{\sigma_{pl}^*}{\sigma_{ys}} \approx 0.44 \left(\frac{\rho^*}{\rho_s} \right). \quad 8.$$

The shear strength can be obtained from the yield criterion. The Deshpande-Fleck yield surface, described below, suggests that the shear strength is 0.69 times the uniaxial strength (43):

$$\tau_{pl}^* = 0.69 \sigma_{pl}^*, \quad 9.$$

or, for open-cell foams, using Equation 5,

$$\frac{\tau_{pl}^*}{\sigma_{ys}} = 0.21 \left(\frac{\sigma^*}{\sigma_s} \right)^{3/2}, \quad 10.$$

and, for closed-cell foams, using Equation 7,

$$\frac{\tau_{pl}^*}{\sigma_{ys}} = 0.23 \left(\frac{\rho^*}{\rho_s} \right)^2 + 0.30 \left(\frac{\rho^*}{\rho_s} \right). \quad 11.$$

In the next section we describe the deformation and failure of metallic foams, modify the models to account for imperfections in their cell structure and compare the results with data for metallic foams.

DEFORMATION AND FAILURE IN METALLIC FOAMS

Compressive stress-strain curves for several aluminum foams are shown in Figure 4a. The shape of the curves is similar to that of the schematic of Figure 3. The initial responses of an open-cell Duocel foam and a closed-cell Alporas foam are shown in more detail in Figure 4b. The Duocel foam is linear elastic: The slopes of the loading and unloading curves are identical. Although the Alporas foam exhibits an initial linear regime (Stage I) at strains of up to about 0.01, the slope of the loading curve is much lower than that of the unloading curve, indicating that there is some plastic deformation even at low strains; similar behavior is observed in the other closed cell foams of Figure 4a. Surface strain mapping reveals that the Duocel material deforms relatively homogeneously until the plateau stress is approached whereas the Alporas material deforms heterogeneously, yielding locally by deformation banding, at stresses of about 1/2 of the plateau stress (Figure 5) (44). The Alporas material strain hardens up to the peak stress (Stage II) and then softens (Stage III).

More detailed surface strain mapping of the incremental distortion in the closed-cell Alporas material at increasing load levels indicates that localized deformation bands become apparent at the onset of nonlinearity (45). The bands are roughly normal to the loading direction and have a width of about one cell-diameter. Within each band, the strain is about an order of magnitude larger than the applied strain while outside the band, the average strains are small, remaining within the elastic range. Some bands that form at the initial nonlinearity in the stress-strain curve harden with further straining so that they become inactive and new bands form. Bands that form close to the peak stress continue to accumulate strain and densify on further loading. Additional bands form at strains beyond the peak stress. The bands are spaced at regular intervals of three to four cell diameters.

The mechanisms of deformation corresponding to the three stages of (I) initial linearity, (II) strain hardening up to the peak stress, and (III) strain softening beyond the peak stress are as follows. In Stage I, local plastic deformations occur within the cell walls, reducing the loading modulus below the unloading modulus. At this stage, strain concentrations are not evident from strain mapping. During Stage II, plastic buckling or bending of the cell walls in weaker cells (ones that are elongated normal to the loading direction or have curved walls) gives rise to deformation bands when the resulting stress concentrations in neighboring cells are sufficient to localize deformation in an entire layer of cells normal to the loading axis. The adjacent cells along the loading axis remain elastic, providing a hardening mechanism that deactivates the deformation band so that it does not immediately produce cell collapse. In Stage III, one of the bands formed in Stage II collapses plastically. As the applied strain increases, the cells adjacent to the collapsed band also buckle, spreading the collapse across the entire section.

Tensile stress-strain curves for three aluminum foams are shown in Figure 6. As in compression, the loading and unloading moduli of the Duocel ERG foam are the

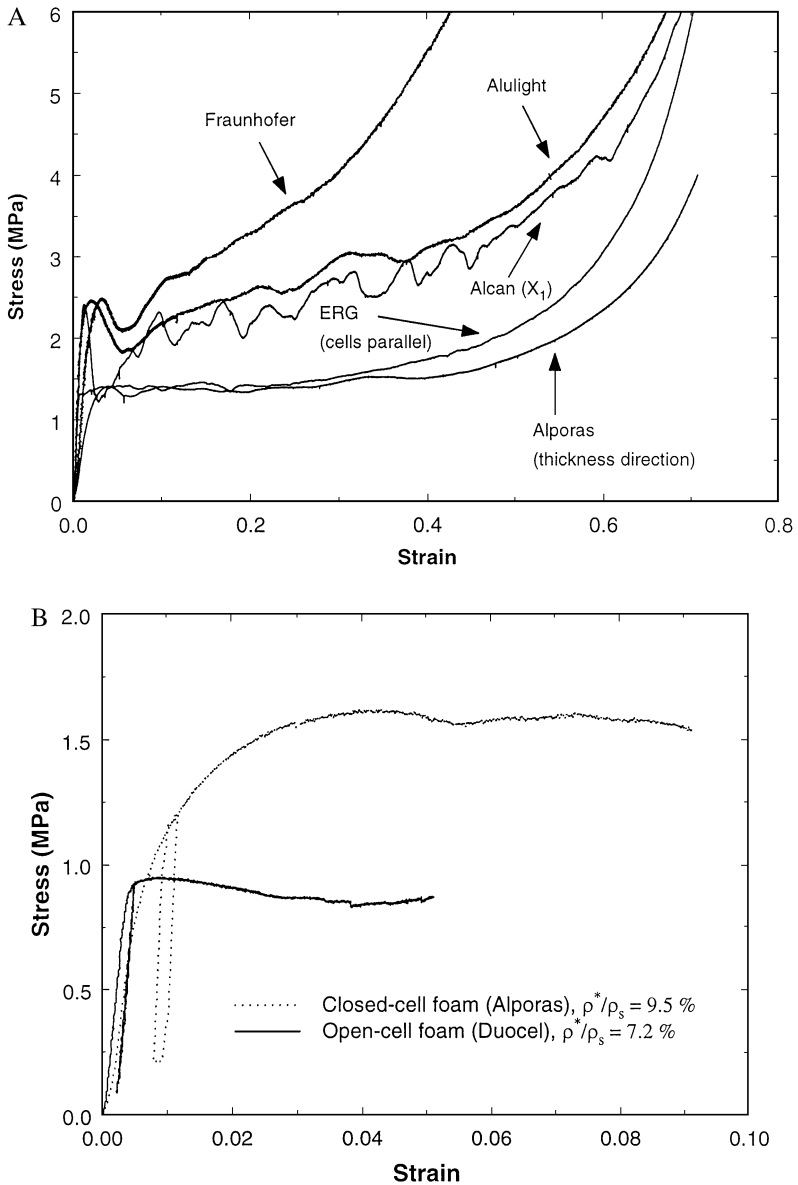


Figure 4 (a) Compressive stress strain curves for aluminum foams showing behavior up to densification (reproduced from 22, with permission of Elsevier Science). (b) Compressive stress strain curves for open-cell Duocel and closed-cell Alporas showing the slopes of the loading and unloading curves (reproduced from 51, with permission of Elsevier Science).

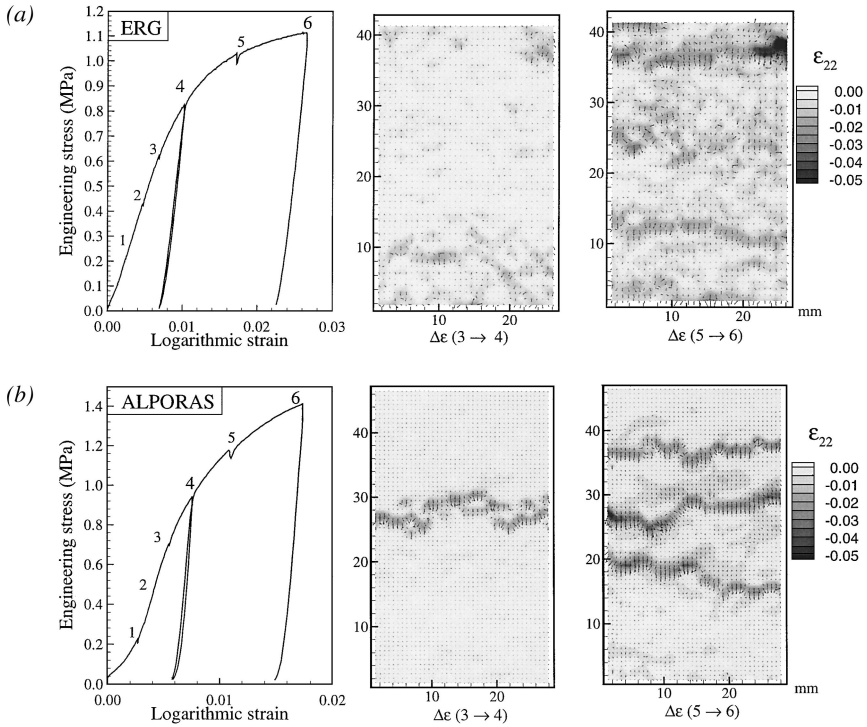


Figure 5 Stress-strain curves and surface strain maps of the incremental principal strains (a) Duocel and (b) Alporas (reproduced from 44, with permission of Elsevier Science).

same while the loading modulus of the Alporas foam is lower than the unloading modulus. The lower loading modulus in the Alporas foam again reflects plastic deformation even within the initial linear region. As the foams yield, they strain harden and fracture at strains of less than 1.5%. The Alcan foam is particularly brittle, fracturing at a strain of about 0.25%. The tensile strength is defined as the maximum stress reached before fracture. A shear stress-strain curve for Alporas aluminum foam is shown in Figure 7. The shear strength is defined as the peak stress.

Data for the unloading Young's modulus from a number of studies are shown in Figure 8, along with lines representing Equations 1 and 3 for open- and closed-cell foams, respectively (21–23, 44, 46–51). The modulus and density data have been normalized by the values for solid aluminum ($E_s = 70$ GPa and $\rho_s = 2.7$ Mg/m³). The data for the open-cell ERG Duocel foam falls close to the line representing Equation 1, as expected. Nearly all the data for the closed-cell foams with relative densities less than 0.3 lie below the line representing Equation 3. Most are closer to the line representing Equation 1, which suggests that bending

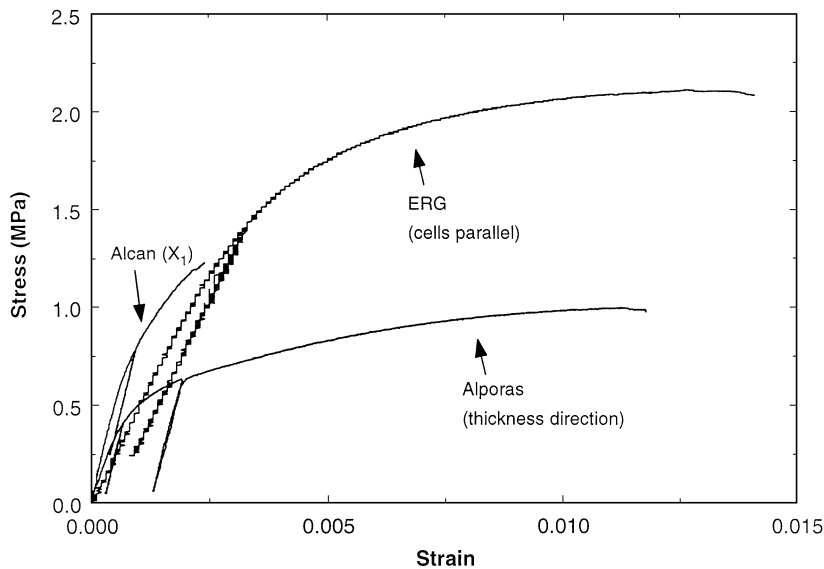


Figure 6 Tensile stress strain curves for aluminum foams (reproduced from 22, with permission of Elsevier Science).

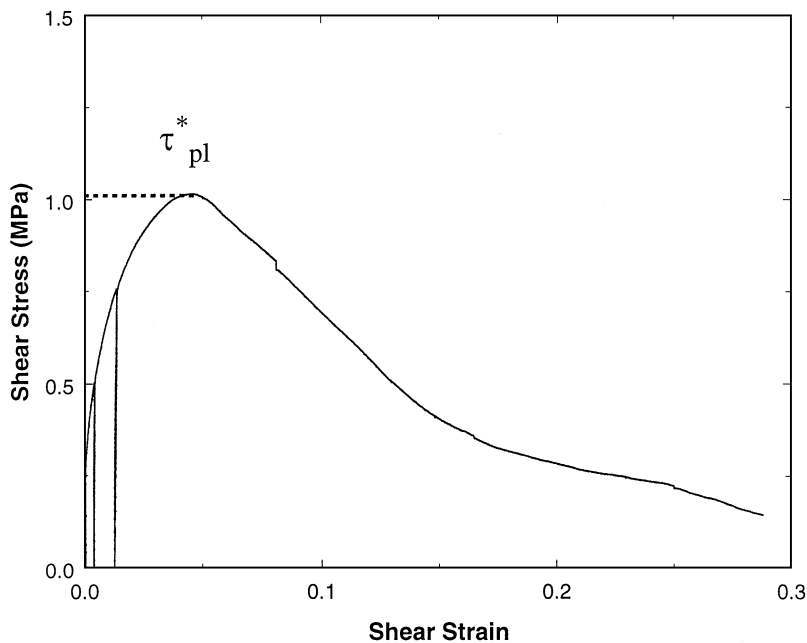


Figure 7 Shear stress strain curve for Alporas aluminum foams (reproduced from 51, with permission of Elsevier Science).

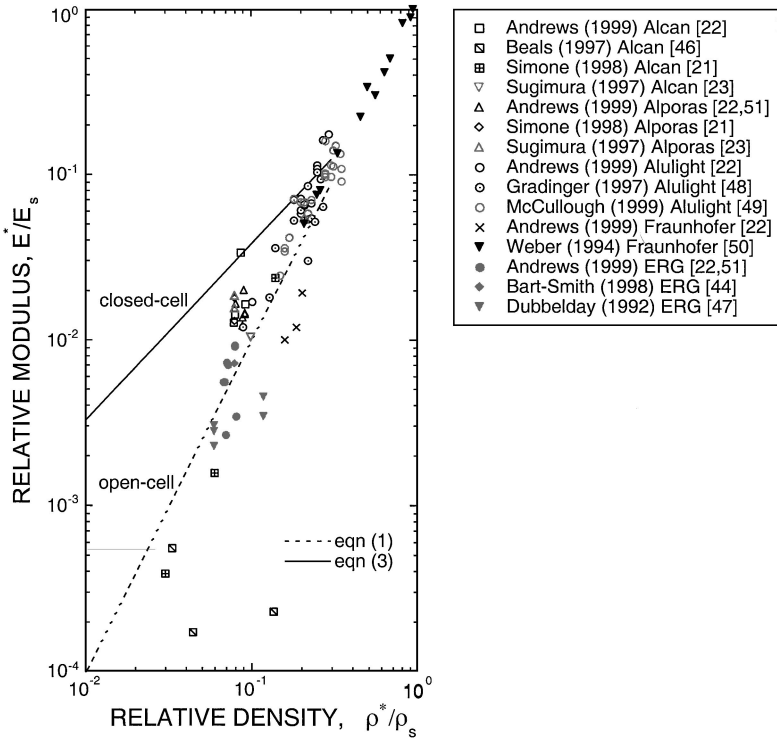


Figure 8 Relative Young's modulus plotted against relative density for aluminum foams. The dashed and solid lines represent Equations 1 and 3, for open- and closed-cell foams, respectively. Beals & Thompson (46) data for loading modulus; Dubbelday (47) and Weber (50) data for vibration test; all other data for unloading modulus.

contributes significantly to the cell wall deformation. Data for the shear moduli are limited: The only available study is that of Dubbelday (52), who found moduli slightly lower than expected from Equation 2, perhaps due to anisotropy in the specimens.

Data for the compressive and tensile strengths of aluminum foams are plotted in Figures 9 and 10, along with lines representing Equations 5 and 7 for open- and closed-cell foams, respectively (21–23, 44, 48–51, 53–59). The strengths have been normalized by the value for the solid alloys (Table 2) (21, 23, 60). Again, the data for the open-cell ERG Duocel foam lie close to Equation 5, as expected, whereas the data for the closed-cell foams lie well below Equation 7 and most are closer to Equation 5, suggesting that plastic bending contributes significantly to the failure. The compressive and tensile strengths are, in general, similar in magnitude. The shear strengths of aluminum foams are plotted in Figure 11, along with lines representing Equations 10 and 11 for open- and closed-cell foams, respectively

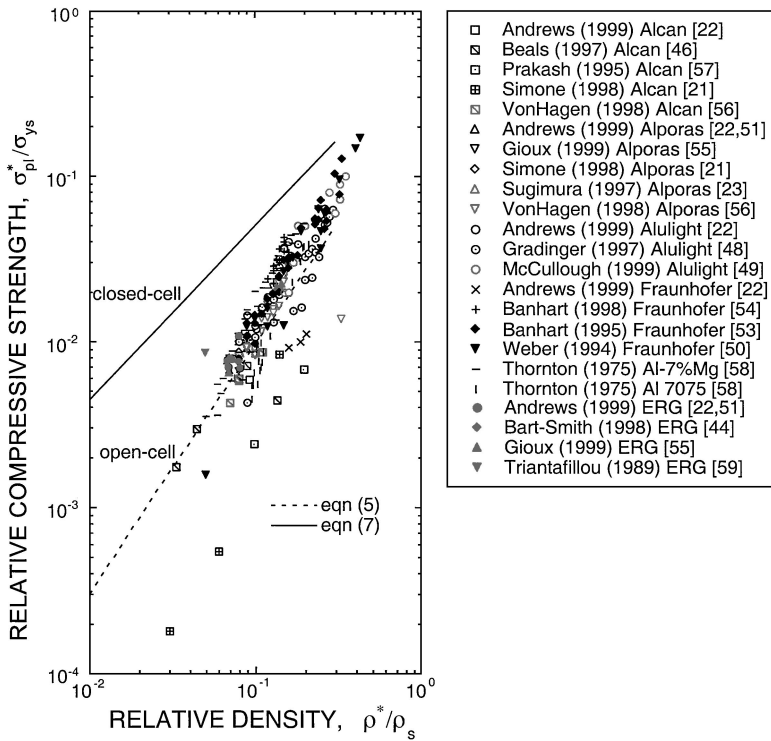


Figure 9 Relative compressive strength plotted against relative density for aluminum foams. The dashed and solid lines represent Equations 5 and 7, for open- and closed-cell foams, respectively. Compressive strength is defined in slightly different ways in different studies; generally it is either the plateau stress or the compressive stress at 20% strain.

(51, 56). The shear strength of the closed-cell foams, like the uniaxial strength, lies close to the line representing the open-cell model, which suggests that plastic bending is again significant.

Bending deformations can arise in closed-cell metallic foams in several ways. Curvature in the cell faces induces bending from both axial and shear forces. Finite element analysis of closed-cell foams with curved cell walls suggests that, for the typical measured cell wall curvatures, the modulus is 60% and the strength is 30% of those for planar faces, which accounts for most of the discrepancy between Equations 3 and 7 and the data (Figures 12 and 13) (22, 40, 61). Irregularities in the cell shape can also induce bending. For instance, observations of the deformations within a closed-cell aluminum foam using computed tomography indicate that the presence of a highly elliptical cell with T-shaped cell wall intersections can induce bending in the neighboring cell walls, initiating the collapse of a deformation band (44). A systematic study of the effect of distortion in

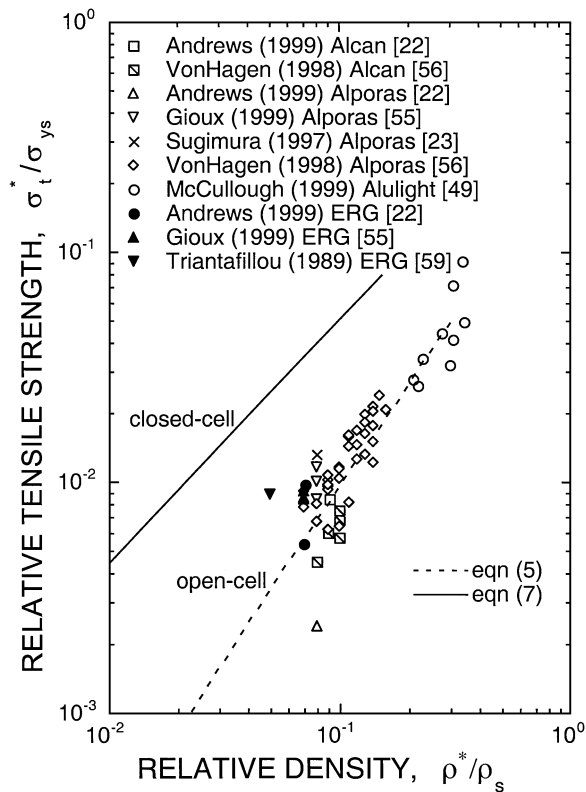


Figure 10 Relative tensile strength plotted against relative density for aluminum foams. The dashed and solid lines represent Equations 5 and 7, for open- and closed-cell foams, respectively.

TABLE 2 Yield strengths of solid cell wall material

Foam	Data source	Yield strength, σ_{ys} (MPa)	Reference source
Alcan	22, 21, 56	390	21
	46	138	Manufacturer literature
	57	—	Normalized data
Alporas	22, 51, 55, 21, 56	172	21
	23	130	23
Alulight	22	250	23
	48	130	21
	49	—	Normalized data
Fraunhofer	22, 13, 53, 50	250	21
ERG	22	193	60
	51, 44, 55, 59	200	

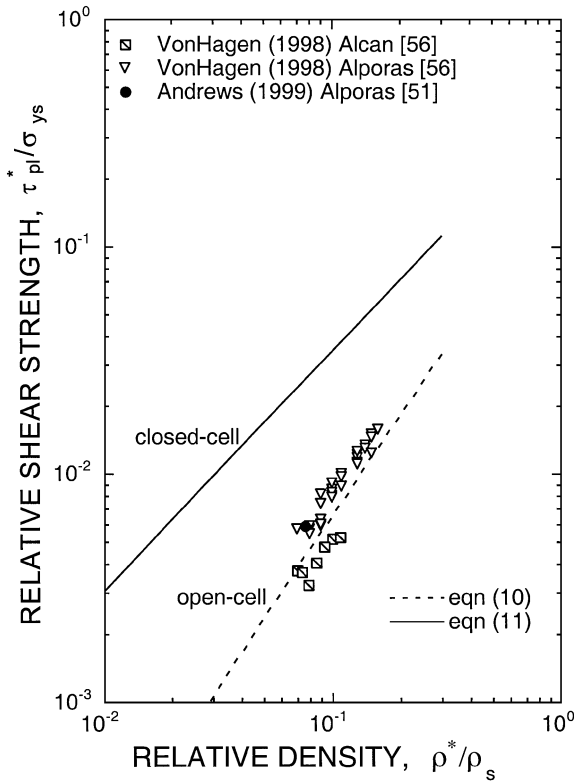


Figure 11 Relative shear strength plotted against relative density for aluminum foams. The dashed and solid lines represent Equations 10 and 11, for open- and closed-cell foams, respectively.

cell shape from a bcc packing of tetrakaidecahedra found that the moduli decreased by about only 10% for even the most distorted shapes (62). The method of distorting the cell shapes in this study does not lead to highly elongated cell shapes; it may be that the elongation of the cell in the former study was important in inducing bending in the cell faces. Fractured cell walls can produce bending. A study of the effect of cell wall fracture on the hydrostatic strength of a periodic, hexagonal honeycomb, in which axial cell wall stretching dominates the intact behavior, found that the hydrostatic strength is reduced to 10% of the intact value by fracture of only 1% of the cell walls (63). Cell collapse is initiated by bending of the cell walls neighboring the fracture sites. Bending was not induced by either a random cell geometry or by non-uniform cell wall thicknesses in closed-cell foams. Closed-cell Voronoi foams have Young's moduli that are close to those for closed-cell, periodic tetrakaidecahedra (29). Changing the cell wall thickness geometry from uniform to Plateau borders has only a slight effect on the modulus and strength of closed-cell tetrakaidecahedral models (39).

The moduli and strengths of the lowest density Alcan foams in Figures 8 and 9 lie well below the lines representing those for open-cell foams: Inhomogeneities in the relative density of the foams within a single specimen also reduce the properties.

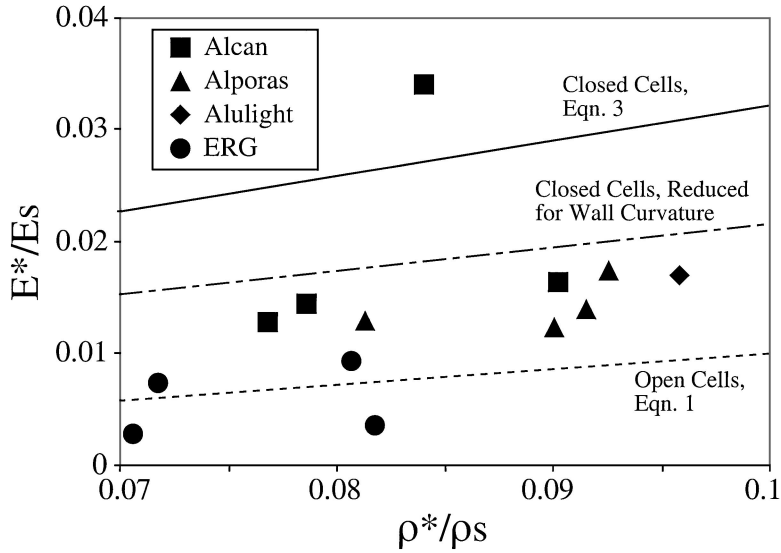


Figure 12 Relative Young's modulus plotted against relative density for specimens on which the cell wall curvature was measured. The dashed-dot line represents the finite element analysis of a closed-cell tetrakaidecahedral model with curved faces (61). All data are for unloading modulus reproduced from 22, with permission of Elsevier Science).

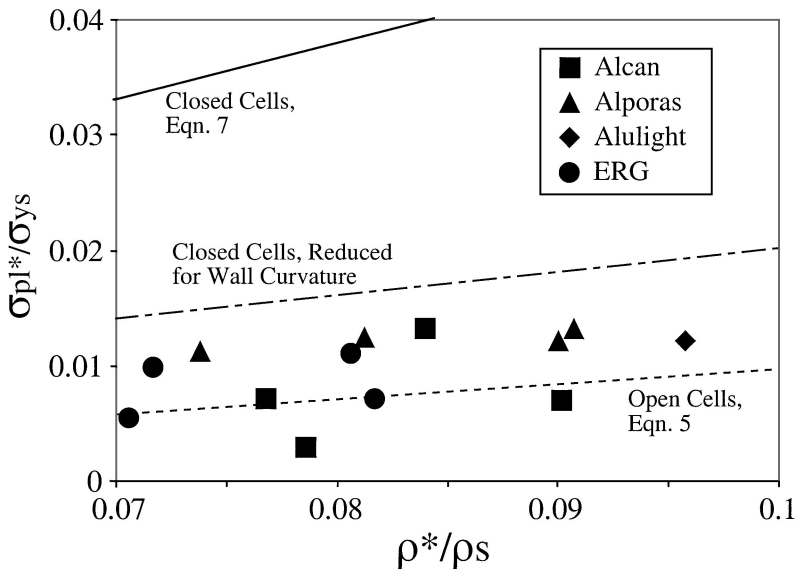


Figure 13 Relative compressive strength plotted against relative density for specimens on which the cell wall curvature was measured. The dashed-dot line represents the finite element analysis of a closed-cell tetrakaidecahedral model with curved faces (21) (reproduced from 22, with permission of Elsevier Science).

For instance, Beals & Thompson (46) report variations in relative density through the thickness of their specimens from 0.033 to 0.14 (the highest values, measured at the bottom of the specimens, result from drainage during processing).

The models summarized in the previous section give a good description of the modulus and strength of open-cell metallic foams. Imperfections in the microstructure of closed-cell metallic foams induce bending in the cell walls, thus reducing their properties to values closer to those of open-cell foams of the same relative density.

SIZE EFFECTS

Size effects arise if the macroscopic dimensions of a specimen or component are of the order of the material's microstructural length scale: For cellular materials, this is the cell size, which, for most metallic foams, ranges from about 2 to 6 mm. In a uniaxial test, the cell edges and faces at the cut surface of the specimen do not carry load, and those close to the cut surface are less constrained than edges and faces within the bulk of the specimen. For large specimens, the surface effects are small and the moduli and strength are close to the bulk values for an infinite specimen. But as the dimensions of the specimen approach those of the cell size, the surface effects become significant, reducing the modulus and strength of the foam. Data for the Young's modulus, normalized by the bulk value for large specimens, are plotted against the ratio of specimen to cell size in Figure 14; the uniaxial compressive strength follows a similar trend (51). Shear tests on metallic foams are usually performed by bonding a long, thin strip of the foam to two rigid plates and attaching the plates to fixtures designed to load the foam along its diagonal. Bonding the surface of the foam to the plates increases the constraint of the cell edges and faces at the surface. As the thickness of the specimen approaches the cell size, surface effects become significant, increasing the shear modulus and strength of the foam. Data for the shear strength, normalized by the bulk value for large specimens, are plotted against the ratio of specimen thickness to cell size in Figure 15 (51). The shear size effect is particularly relevant to the design of structural sandwich panels with metallic foam cores because aerospace applications may require that the panels be relatively thin, of the order of 5–15 mm, or roughly one to four cell sizes.

The microstructural origins of the different size effects have been modeled for a regular hexagonal elastic-plastic honeycomb (64). The honeycomb has two attractive features: Its cell walls bend and form plastic hinges, similar to metallic foams, and its periodic structure allows it to be more easily analyzed than a foam. The Young's moduli and uniaxial strength of an infinitely long honeycomb were calculated as a function of the ratio of the width of the honeycomb to the cell size. The Young's modulus is affected both by the length of the cut cell wall at the boundary and by the reduced constraint of the next outermost layers of cells. The uniaxial strength of honeycombs with no cut cell walls at the boundary (with widths equal to an integer number of hexagonal cells) is constant; the reduced constraint near the boundary has no effect on the uniaxial strength. For honeycombs with cut

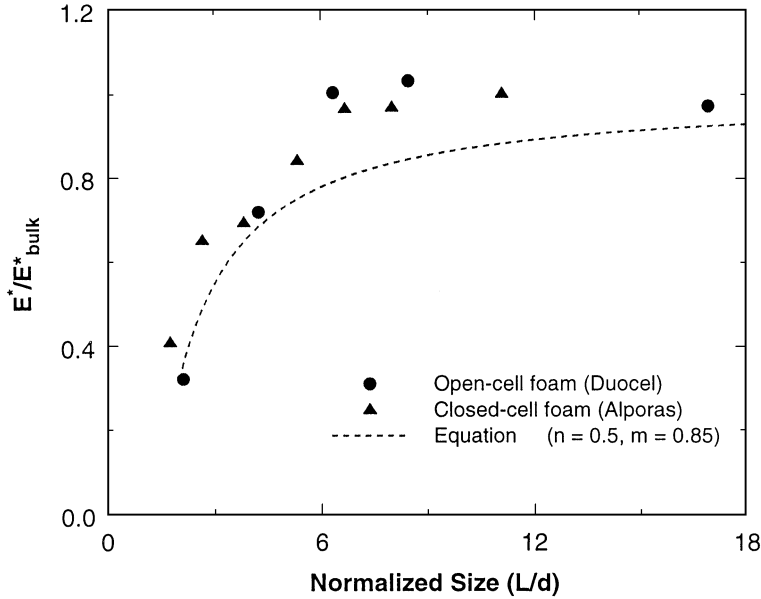


Figure 14 The Young's modulus, E^* , normalized by that for large specimens, E^*_{bulk} , plotted against the ratio of the specimen size, L , to the cell size, d . The modulus reaches a plateau level at about $L/d = 6$ for both the open- and the closed-cell foams. The dashed line represents the rule of mixtures model described in the text (reproduced from 51, with permission of Elsevier Science).

walls at the boundary, the uniaxial strength is reduced as the size of the specimen decreases due to the increased area fraction of stress-free cell walls. Overall, the Young's modulus is expected to decrease more rapidly than the uniaxial strength as the ratio of the specimen to the cell size decreases.

The shear size effect has been calculated by considering an infinitely long honeycomb with a thickness equal to an integer number of cells bonded to rigid plates. The length of the vertical cell walls rigidly attached to the plates is allowed to vary from 0 to ℓ . The results can be summarized by considering two cases. In the first, the cut in the vertical cell wall is made so that the length of the vertical wall at one rigid plate is ℓ whereas that at the other rigid plate is zero. In this case, the ratio of the specimen thickness to the cell size has a negligible effect on the shear modulus and strength of the honeycomb. In the second case, the vertical walls are both of length $\ell/2$. For this symmetrical case, the shear modulus and strength increase as the ratio of the specimen thickness to the cell size decreases. The effect is of short range: The shear modulus approaches the bulk value if the specimen thickness is greater than about three times the cell size, and the shear strength equals the bulk value if the specimen thickness is equal or greater than twice the cell size.

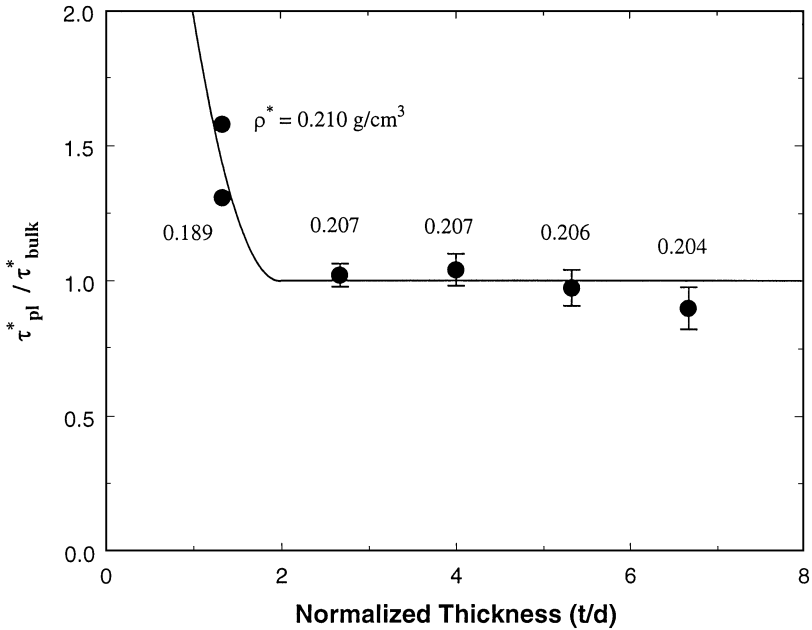


Figure 15 The shear strength, τ_{pl}^* , normalized by that for thick specimens, τ_{bulk}^* plotted against the ratio of the specimen thickness, t , to the cell size, d (Alporas). The strength reaches the plateau level for $t/d = 2$ (reproduced from 51, with permission of Elsevier Science).

Size effects in foams can be estimated by considering the mechanisms identified in the analytical study of honeycombs. For instance, the Young's modulus can be estimated using a simple rule of mixtures approach. Well away from the outer surface, the material has the Young's modulus of the bulk. Surrounding this core, there is a layer of lower stiffness, reflecting the reduced constraint near the surface. And at the surface, there is a layer of cut cell edges with zero stiffness. The line shown in Figure 14 reflects a stiffness of the reduced constraint layer of 0.85 of the bulk value, a thickness of the reduced constraint layer of one half the cell size, and a thickness of the cut cell layer of one fourth the cell size. The size effect for the shear strength of a foam is the same as that for a honeycomb because there are no stress or strain gradients in the out-of-plane direction when the foam is wide enough. The line shown in Figure 15 reflects this.

In summary, the reduced constraint and unloaded cell walls at the edges of a uniaxial foam specimen reduce the Young's modulus and compressive strength as the ratio of the specimen size to the cell size is reduced below roughly eight. The increased constraint on the cell walls of a foam bonded to rigid loading platens in a shear test (or in foam core of a sandwich panel) increases the shear strength if the ratio of the thickness to the cell size is reduced below two.

YIELD CRITERIA

Metallic foams can be subject to multiaxial loading in sandwich panels and in energy absorption devices. A yield criterion, giving the combination of stresses required for failure, is then required. For porous materials such as foams, yield depends on both the equivalent stress, σ_e , and the mean stress, σ_m . Consider an idealized open-cell foam with a tetrakaidecahedral unit cell. Under shear loading, the cell edges bend and form plastic hinges, so that the shear strength varies as $(\rho^*/\rho_s)^{3/2}$, like the uniaxial strength. Under hydrostatic loading, the cell edges either extend or contract uniaxially so that the hydrostatic strength varies with (ρ^*/ρ_s) . [Note that an elastic analysis of the open-cell tetrakaidecahedral model shows that the cell edges axial stretch, rather than bend, and that the bulk modulus of varies linearly with density (38).] In the limit of zero mean stress, failure occurs when the equivalent stress equals the uniaxial stress. In the limit of hydrostatic stress, the foam fails when the mean stress is equal to $\frac{1}{3}(\frac{\rho^*}{\rho_s})$. Combining these gives (65)

$$\pm \frac{\sigma_e}{\sigma_{pl}} + 0.81 \left(\frac{\rho^*}{\rho_s} \right) \left(\frac{\sigma_m}{\sigma_{pl}^*} \right)^2 = 1. \quad 12.$$

The yield surface for the ideal foam is highly elongated, reflecting the bending failure of the cell edges in pure shear and the axial failure of the cell edges in hydrostatic loading. In practice, real foams have imperfections in their structures that induce bending for all stress states, which contract the yield surface along the hydrostatic axis.

Two phenomenological yield criteria for porous materials have recently been applied to metallic foams. The first, based on the Drucker-Prager criterion, accounts for unequal uniaxial tensile and compressive strengths (66):

$$f = \sigma_e - \gamma p + \frac{\alpha'}{d_0 \sigma_c^*} p^2 - d_0 \sigma_c^*, \quad 13.$$

where σ_c^* is the uniaxial compressive strength, p is the hydrostatic pressure [$P = -\frac{1}{3}(\sigma_1 + \sigma_2 + \sigma_3)$] and the constants γ , α' , and d_0 depend on the ratio of the uniaxial compressive-to-tensile strengths and the plastic Poisson's ratio. It is interesting to note that the Miller criterion (Equation 13) can be obtained from the derivation for the criterion for the ideal foam (Equation 12) by accounting for bending stresses that are induced in the cell edges due to cell wall curvature, even under a pure hydrostatic loading.

The second, based on a powder compaction model, gives an elliptical yield surface (43):

$$\Phi \equiv \hat{\sigma} - \sigma_{pl}^* \leq 0, \quad 14.$$

where

$$\hat{\sigma}^2 = \frac{1}{1 + (\alpha/3)^2} [\sigma_e^2 + \alpha^2 \sigma_m^2],$$

and α defines the aspect ratio of the elliptical yield surface. The plastic Poisson's ratio depends on α according to:

$$\nu^P = \frac{\frac{1}{2} - \left(\frac{\alpha}{3}\right)^2}{1 + \left(\frac{\alpha}{3}\right)^2}. \quad 15.$$

Measured values of the plastic Poisson's ratios are close to zero for metallic foams (for instance, for 8% dense Alporas, $\nu^P = 0.024$), giving $\alpha \sim 2$. A similar yield criterion has been proposed for polymeric foams by Zhang et al (67).

The yield criteria are compared with data for failure of metallic foams under triaxial loading in Figures 16 and 17. All three yield surfaces are shown in Figure 16 along with data for roughly 8% dense Alporas aluminum foam. The yield surface for the ideal foam (Equation 12) is highly elongated along the hydrostatic axis, grossly overestimating the strength of the foams when the mean stress is significant. Miller's yield surface (Equation 13) reflects the slightly different strengths of the foam in tension and compression. The Miller criterion suffers from the problem that the yield surface comes to a point for hydrostatic loading so that calculation of the plastic strain rate assuming normality becomes difficult. The Deshpande-Fleck criterion (Equation 14) avoids this problem, gives the best description of the data, and is simpler than the Miller criterion; for these reasons

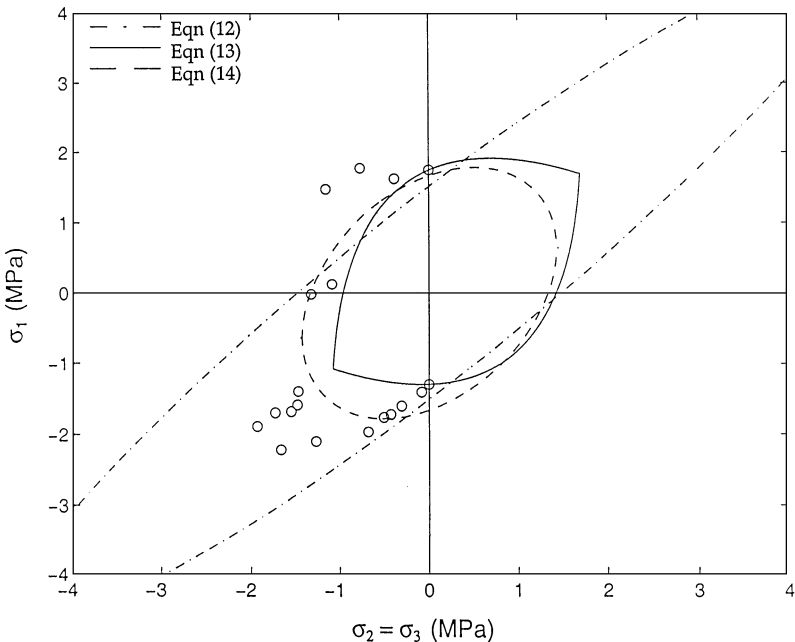


Figure 16 Triaxial yield data for 8% dense Alporas foam. Axial stress, σ_1 , is plotted against radial stress, $\sigma_2 = \sigma_3$ (reproduced from 55, with permission of Elsevier Science).

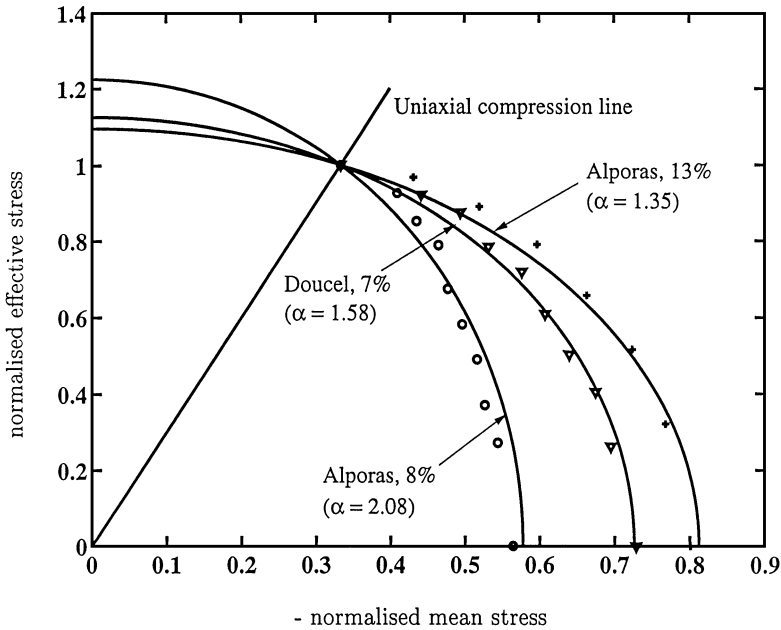


Figure 17 Initial yield surfaces for three aluminum foams. The stresses have been normalized by the uniaxial yield strength. The lines corresponding to Equation 14 for the values of α are shown (reproduced from 43, with permission of Elsevier Science).

it is currently being widely adopted for metallic foams. Data for three aluminum foams are compared with the Deshpande-Fleck criterion in Figure 17: Agreement is excellent. The scatter in the data of Figure 17 is less than that in Figure 16. Each set of data points for one material in Figure 17 was obtained from a single specimen; multiple stress states producing yield were applied to that specimen, eliminating inter-specimen variability. The data in Figure 16 correspond to a different test specimen for each stress state.

CREEP

The use of metallic foams as cores for high-temperature sandwich structures requires an understanding of their creep behavior. The steady-state secondary creep rate of an open-cell foam can be calculated from the creep-bending response of a cell edge (68). Let the creep rate $\dot{\epsilon}$ of the solid cell wall material under a stress σ be described by

$$\dot{\epsilon} = \dot{\epsilon}_0 \left(\frac{\sigma}{\sigma_0} \right)^n, \quad 16.$$

where $\dot{\epsilon}_0$, σ_0 , and n are constants characterizing the creep of the solid material of which the cell walls are made. The parameter $\dot{\epsilon}_0$ incorporates the temperature dependency through the Arrhenius relationship

$$\dot{\epsilon}_0 = C \exp\left(-\frac{Q}{RT}\right), \quad 17.$$

where C is a constant, Q is the activation energy for the creep process, R is the gas constant and T is the absolute temperature. The deflection of a cantilever beam of length ℓ , cross-section t^2 , loaded at the end by a force, F , and made from a material obeying Equation 16 is proportional to

$$\delta \propto \frac{1}{n+2} \dot{\epsilon}_0 \frac{\ell^2}{t} \left[\left(\frac{2n+1}{n} \right) \frac{F\ell}{\sigma_0 t^3} \right]^n. \quad 18.$$

Dimensional arguments give $F \propto \sigma^* \ell^2$, $\dot{\epsilon}^* \propto \delta/\ell$, and the relative density $\rho^*/\rho_s \propto (t/\ell)^2$. Combining these expressions gives the creep rate for the foam, $\dot{\epsilon}^*$ under an applied stress σ^* :

$$\frac{\dot{\epsilon}^*}{\dot{\epsilon}_0} = \frac{C_4}{(n+2)} \left(\frac{C_5(2n+1)}{n} \frac{\sigma^*}{\sigma_0} \right)^n \left(\frac{\rho_s}{\rho^*} \right)^{\frac{3n+1}{2}}, \quad 19.$$

The constants C_4 and C_5 are found by considering two limits. At the limit of $n \rightarrow \infty$ (with σ_0 replaced by σ_{ys}) the equation reduces to that for plastic collapse (Equation 5). And at the limit of $n = 1$ (with $\sigma_0/\dot{\epsilon}_0$ replaced by E_s) it reduces to that for linear elasticity (Equation 1). The final result for the creep of open-cell foams is

$$\frac{\dot{\epsilon}^*}{\dot{\epsilon}_0} = \frac{0.6}{(n+2)} \left(\frac{1.7(2n+1)}{n} \frac{\sigma^*}{\sigma_0} \right)^n \left(\frac{\rho_s}{\rho^*} \right)^{\frac{3n+1}{2}}. \quad 20.$$

The secondary strain rate of open cell foams depends on σ_0 and $\dot{\epsilon}_0$ in the same way as the solid so that the foam has the same power law exponent n and activation energy Q as the solid. The strain rate is highly sensitive to the foam density, varying as $(\rho^*/\rho_s)^{-\frac{3n+1}{2}}$.

Closed cell foams have faces that carry membrane stresses when the foam deforms. If the faces are flat and are of thickness t_f , their creep rate is

$$\dot{\epsilon} \approx \dot{\epsilon}_0 \left(\frac{3}{2} \frac{\sigma^* \ell}{\sigma_0 t_f} \right)^n, \quad 21.$$

and the steady-state creep rate of the closed cell foam is

$$\frac{\dot{\epsilon}^*}{\dot{\epsilon}_0} = \left[\frac{\sigma^*/\sigma_0}{\frac{1}{1.7} \left(\frac{n+2}{0.6} \right) \left(\frac{n}{2n+1} \right) \left(\phi \frac{\rho_s^*}{\rho_s} \right)^{\frac{3n+1}{2n}} + \frac{2}{3} (1-\phi) \frac{\rho_s^*}{\rho_s}} \right]^n \quad 22.$$

where ϕ is the fraction of the solid in the cell edges. When all the solid is in the edges ($\phi = 1$), Equation 22 reduces to Equation 20. But when the faces are flat and of uniform thickness, ($\phi = 0$), it reduces instead to Equation 21.

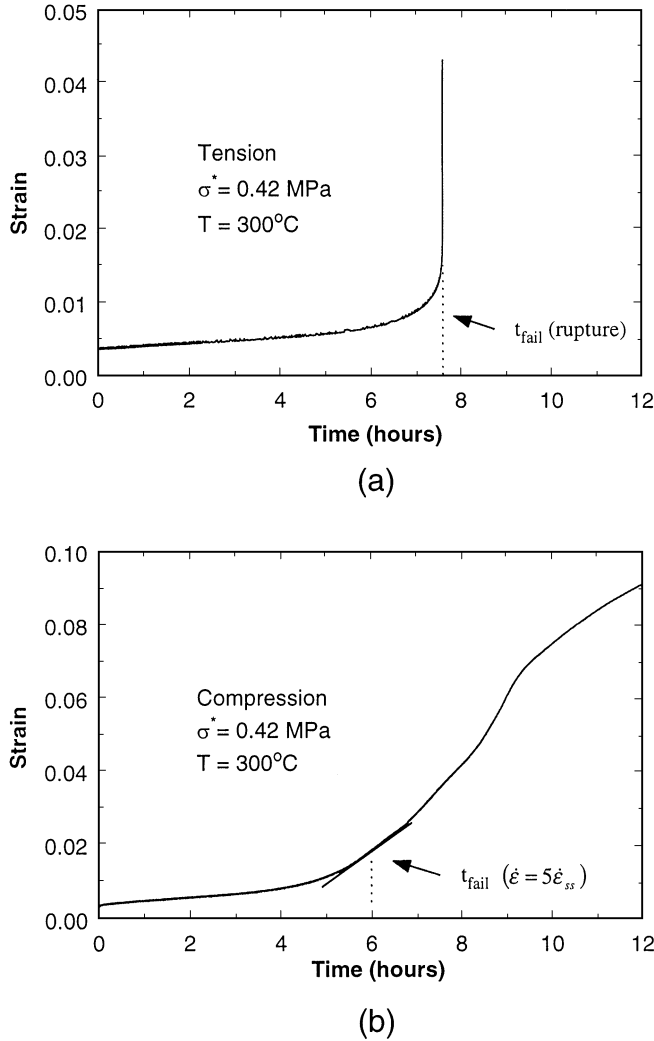


Figure 18 Strain plotted against time for creep tests on an open-cell aluminum foam (Duocel, ERG): (a) tension, (b) compression (reproduced from 68, with permission of Elsevier Science).

Typical plots of strain against time for a 9% dense open-cell aluminum foam (Duocel, ERG) loaded in tension and in compression are shown in Figure 18. In tension, the secondary creep regime is followed by tertiary creep and rupture. In compression, the progressive failure of bands of cells leads to an increase and then a decrease in the slope of the curve in the tertiary regime as subsequent layers of cells collapse. The secondary rate is plotted against stress and

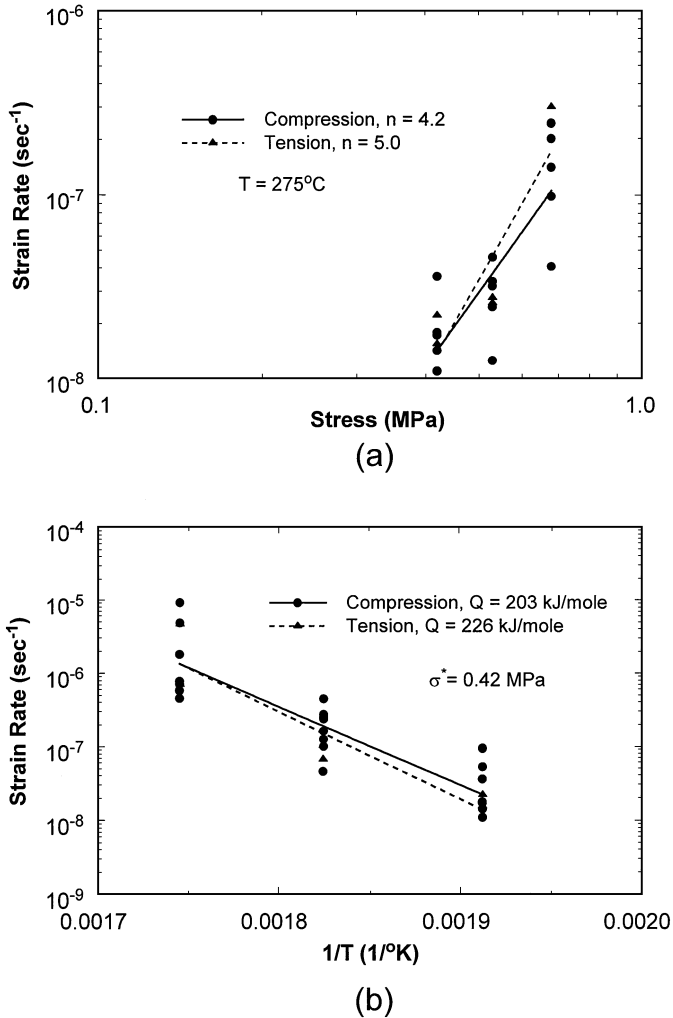


Figure 19 Secondary creep strain rate plotted against (a) stress at constant temperature and (b) $1/\text{temperature}$ at constant stress for an open-cell aluminum foam (Duocel, ERG) (reproduced from 68, with permission of Elsevier Science).

against $1/\text{temperature}$ is Figure 19: The measured values of the exponent n and the activation energy Q are similar to those for the solid alloy, as expected (6101-T6, $n = 4.0$, $Q = 173 \text{ kJ/mole}$). The dependence of creep rate on relative density is shown in Figure 20: the value of the slope of -6.5 given by Equation 20 (slope $= -6.5$ for $n = 4$) compares well with the measured value of -6.4 . The model gives a good description of the creep of this open-cell aluminum foam. The time to failure was found to be well described by the Monkman-Grant relationship (69).

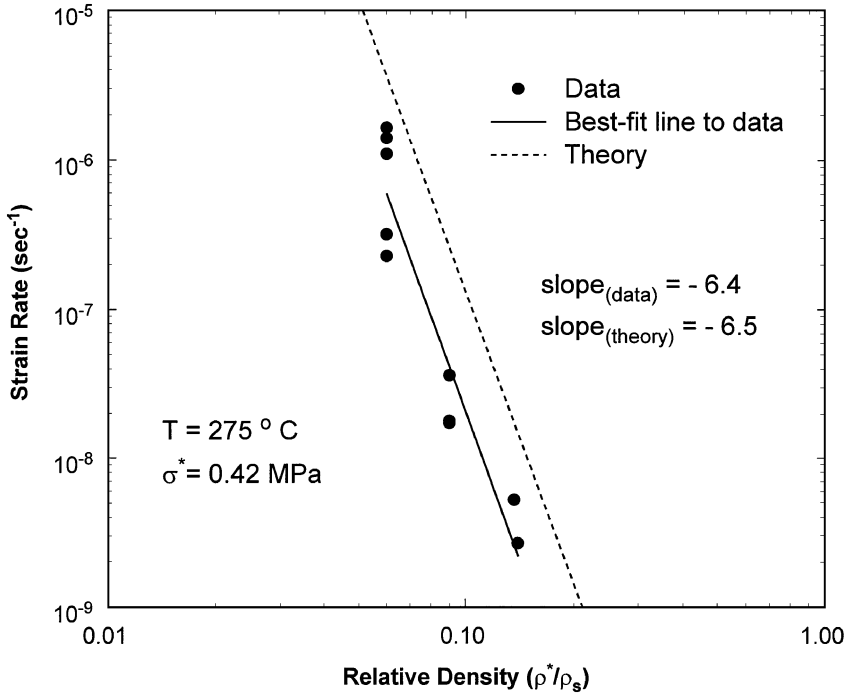
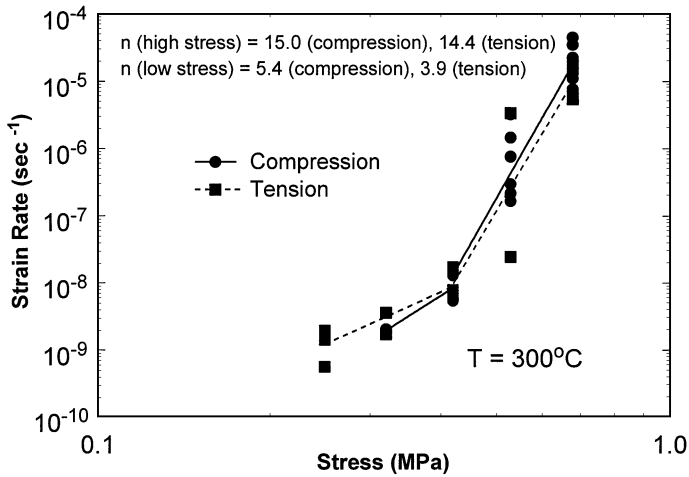
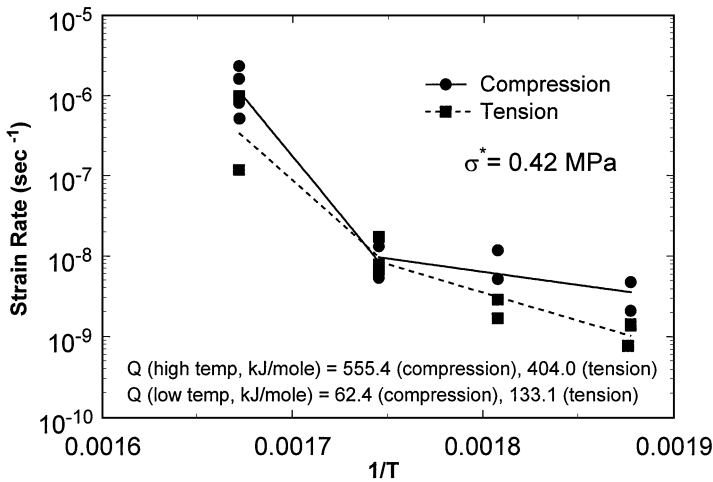


Figure 20 Secondary creep strain rate plotted against relative density at constant stress and temperature for an open-cell aluminum foam (Duocel, ERG) (reproduced from 68, with permission of Elsevier Science).

Data for the creep of a 9% dense closed-cell aluminum foam (Alporas) are shown in Figure 21 (70). At slow stresses and temperatures, the exponent n and the activation energy Q are close to those expected for aluminum and its alloys. (The creep properties of the solid cell wall material are not known since it is not a standard aluminum alloy, and it is difficult to measure the creep properties of individual cell walls.) At high stresses and temperatures, the exponent n and the activation energy Q are much higher. One possible explanation is that local stress concentrations give rise to power law breakdown in some cell walls, effectively unloading them. The process has been modeled in a two-dimensional honeycomb by assuming that a threshold stress must be reached before power law breakdown occurs and that the number of struts undergoing power law breakdown increases with the applied stress. The result of the simulation is shown in Figure 22: below the threshold stress, the material has an n value identical to that for the solid cell wall material ($n = 4.4$) while above it, n increases dramatically. The simulation also accounts for an increase in the activation energy above that for the solid cell wall material.



(a)



(b)

Figure 21 Secondary creep strain rate plotted against (a) stress at constant temperature and (b) 1/temperature at constant stress for a closed-cell aluminum foam (Alporas) (reproduced from 70, with permission of Elsevier Science).

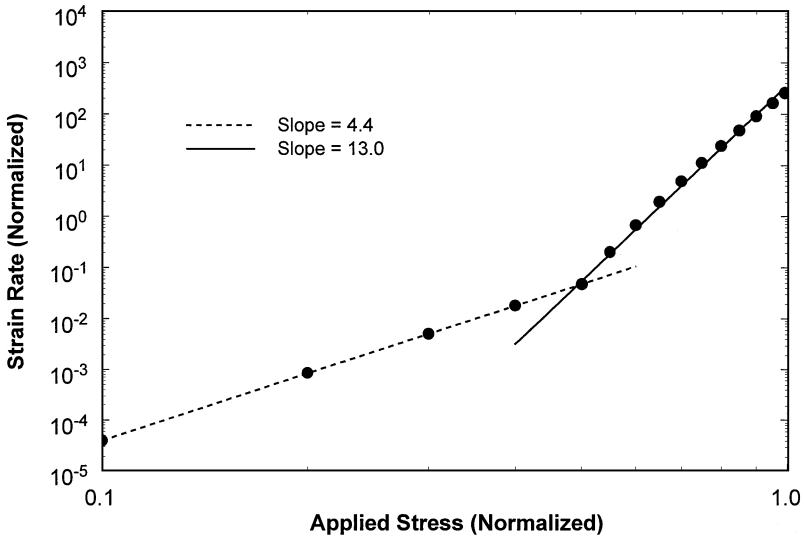


Figure 22 Results of a simulation of creep in a honeycomb in which, above a threshold stress, increasing numbers of cell walls undergo power law breakdown, effectively unloading them, (reproduced from 70, with permission of Elsevier Science).

FATIGUE

In many structural applications, metallic foams may be subjected to repeated loadings, requiring a knowledge of the number of cycles to fatigue failure, N_f , under a given stress range $\Delta\sigma$. For tension-tension loading, the fatigue life is defined as the number of cycles for separation of the specimen, whereas for compression-compression, it is that for initial crushing. The main papers on fatigue of metal foams are those of Sugimura et al (71), Harte et al (72), and McCullough et al (73): Their results are summarized here.

Typical plots of the elongation and shortening of two aluminum foams, one open cell (Duocel, ERG), the other closed cell (Alporas), under tension-tension and compression-compression fatigue are shown in Figure 23 (72). The load ratio R is defined as $R = |\sigma_{\min}|/|\sigma_{\max}|$. In both tension-tension and compression-compression there is an initial increase in strain (stage I), followed by a plateau, in which many cycles elapse with little increase in strain (stage II). At a critical number of cycles, N_T , the strain increases sharply (stage III). In both tension-tension and compression-compression, fatigue failure occurs at a strain of about 2%.

In tension-tension the mechanism of progressive lengthening (stage II) is thought to be a combination of cyclic ratchetting and low-cycle fatigue of the cell edges (and faces in the case of closed-cell foams). The strain increases sharply (stage III) when a macroscopic crack initiates and propagates across the section of the specimen.

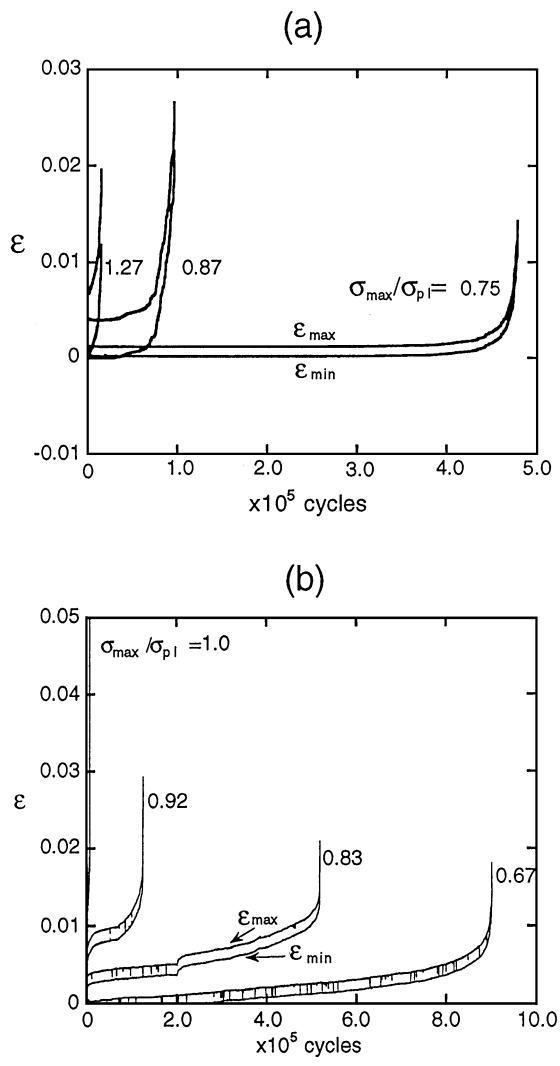


Figure 23 Progressive lengthening (a, b) or shortening (c, d) of aluminum foams in tension-tension or compression-compression fatigue. (a, c) seven percent dense Duocel (ERG), (b, d) 11% dense Alporas. (e) Schematic of compressive-compressive fatigue shortening curve, showing three stages described in the text. (a–d) reproduced from (72); (e) reproduced from 71, with permission of Elsevier Science).

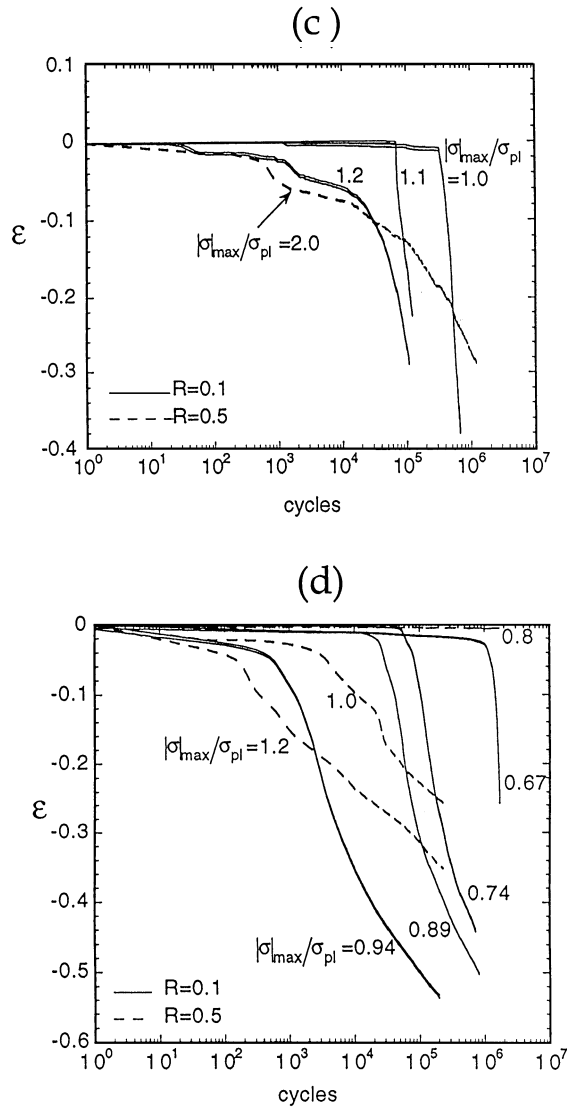


Figure 23 (Continued)

In compression-compression the mean compressive strain increases slowly up to a value of about 2%, at which point the strain increases much more rapidly. In the open-cell foam, the rapid stage III strain accumulation occurs uniformly throughout the specimen. Failure is by low-cycle fatigue of the cell edges, resulting in debris consisting of tetragonal joints. In the closed-cell foam the stage II strain accumulation corresponds to the early stages of the formation of a crush band across the specimen. Just before the formation of the initial crush band, cell faces aligned

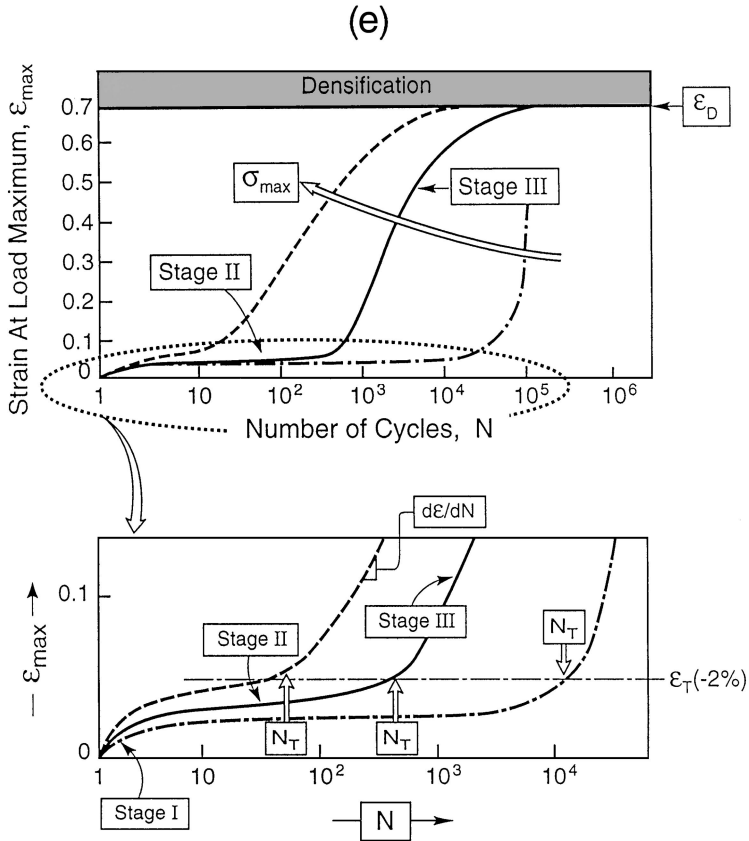
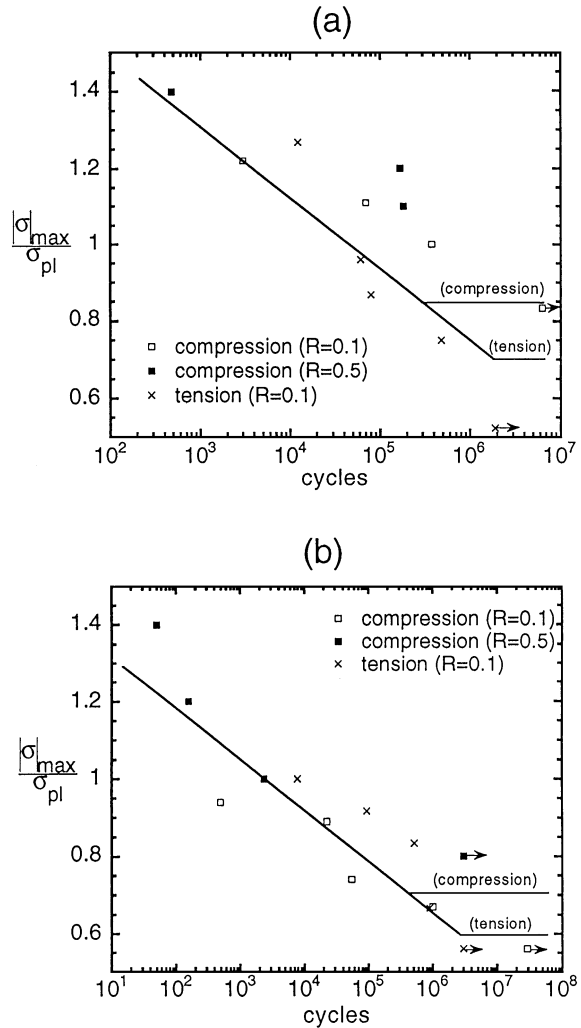


Figure 23 (Continued)

with the loading direction are observed to buckle plastically. The critical number of cycles at which stage III begins, N_T , corresponds to the first fully developed crush band. The rapid stage III strain accumulation is due to progressive crushing either by the broadening of a single crush band or by the sequential formation of separate crush bands, depending on the homogeneity of the specimen. In less homogeneous specimens, the crush bands form preferentially from large cells (71). Failure is by plastic bending and buckling of the cell edges and faces along with tensile cracking of some cell faces. The differing localization responses of the open- and closed-cell foams reflect those in a monotonic test.

S-N curves for both foams are shown in Figure 24 (72). The maximum stress in the fatigue loading is normalized by the plateau stress, defined by the 10% offset strain. The endurance ratio is defined as the ratio of $\sigma_{\max}/\sigma_{pl}$ at a fatigue life of 10^7 cycles: it is about 0.7 in tension-tension and about 0.8 in compression-compression for the open-cell foam and is slightly lower for the closed-cell foam. The study of McCullough et al (73) on low- and high-density specimens of different alloys

Figure 24 S-N curves for tension-tension fatigue and compression-compression fatigue of (a) 7% dense Duocel (ERG) and (b) 11% dense Alporas. The maximum stress in the fatigue cycle is normalized by the 2% offset yield stress (reproduced from 72, with permission of Elsevier Science).



Alulight foam gives further insights. The S-N curve for higher density specimens lies above that for lower density specimens, giving the higher density specimens a higher endurance limit. The lower the ductility of the foam, the lower the endurance limit.

CONCLUSIONS

Metallic foams have a combination of properties that make them attractive for lightweight structural sandwich panels, energy absorption devices, and heat dissipation devices. The recent development of a variety of processes for making

metallic foams with improved properties at lower cost has led to increased interest in their use in engineering components. A number of studies have led to an improved understanding of the mechanisms of deformation and failure in metallic foams. Their response to multiaxial, creep, and fatigue loading has recently been characterized for the first time. This improved understanding of the mechanical response of metallic foams, combined with structural optimization design strategies, provides a foundation for their use in engineering applications.

ACKNOWLEDGMENTS

The author would like to acknowledge the financial support of the ARPA MURI Ultralight Metal Structures Contract Number N00014-96-1-1028. Discussions with a number of collaborators on that project have been insightful. I would particularly like to thank: Professors MF Ashby and NA Fleck of the Cambridge University Engineering Department; Professor JW Hutchinson of the Division of Engineering and Applied Sciences, Harvard University; Professor AG Evans of the Materials Research Institute, Princeton University; Professor RE Miller of the Department of Mechanical Engineering, University of Saskatchewan; Dr P Onck of Micromechanics of Materials, Delft University of Technology; Drs E Andrews, L Crews, AE Simone, and G Gioux, TM McCormack, and W Sanders of the Massachusetts Institute of Technology.

Visit the Annual Reviews home page at www.AnnualReviews.org

LITERATURE CITED

1. Gibson LJ, Ashby MF. 1997. *Cellular Solids: Structure and Properties*, Cambridge, UK: Cambridge Univ. Press, 2nd ed.
2. Ashby MF, Evans AG, Fleck NA, Gibson LJ, Hutchinson JW, Wadley HNG. 2000. *Metal Foams: A Design Guide*. London: Butterworths. In Press
3. Banhart J, Baumeister J, Melzer A, Seeliger W, Weber M. 1998. *Metall.* 52(12):726–29. (in German)
4. Davies GJ, Zhen S. 1983. *J. Mater. Sci.* 18:1899–911
5. Evans AG, Hutchinson JW, Ashby MF. 1999. *Prog. Mater. Sci.* 43(3):171–221
6. Elliot JC. 1956. *U.S. Patent No. 2751289*
7. Thiele W. 1972. *Met. Mater.* 6:349–52
8. Gergely V, Clyne TW. 1998. *The effect of oxide layers on gas-generating hydride particles during production of aluminum foams.* Proc. Mater. Res. Soc. Symp. 521:139–44
9. Gergely V, Clyne TW. 1999. *A novel route to aluminum foam roduction.* Proc. Met. Foam '99. Bremen, Germany. In press
10. Akiyama S, Imagawa K, Kitahara A, Nagata S, Morimoto K, et al. 1987. *U.S. Patent No. 4,713,277*
11. Jin I, Kenny L, Sang H. 1990. *U.S. Patent No. 4,973,358*
12. Ruch W, Kirkevag B. 1990/1991. *Int. Patent Appl.: PCTIN09010115, WO 91101387*
13. Banhart J, Baumeister J. 1998. *Production methods for metallic foams.* Proc. Mater. Res. Soc. Symp. 521:121–32
14. Degischer HP. 1997. *Mater. Design* 18(4/6):221–26
15. Simancík F, Jerz J, Kovácik J, Minar P. 1997. *Kovove Mater.* 35:265–77
16. Martin RL. 1996. *U.S. Patent No. 5,564,064*

17. Schwartz DS, Shih DS, Lederich RJ, Martin RL, Deuser DA. 1998. *Development and scale up of the low density core process for Ti-64*. Proc. Mater. Res. Soc. Symp. 521:225–30
18. Uslu C, Lee KJ, Sanders TH, Cochran JK. 1997. *Ti-6Al4V hollow sphere foams in synthesis/processing of lightweight metallic materials II*. Warrendale, PA: Min. Met. Mater. Soc.
19. Shapovalov VI. 1991. *MRS Bull.* 19(4):24–28
20. Shapovalov VI. 1998. *Formation of ordered gas-solid structures via solidification in metal-hydrogen systems*. Proc. Mater. Res. Soc. Symp. 521:281–90
21. Simone AE, Gibson LJ. 1998. *Acta Mater.* 46:3109–23
22. Andrews EW, Sanders W, Gibson LJ. 1999. *Mater. Sci. Eng. A* 270:113–24
23. Sugimura Y, Meyer J, He MY, Bart-Smith H, Grenestedt J, Evans AG. 1997. *Acta Mater.* 45(12):5245–59
24. Ko WL. 1965. *J. Cell. Plast.* 1:45
25. Patel MR, Finnie I. 1970. *J. Mater.* 5:909
26. Menges G, Knipschild F. 1975. *Polymer Eng. Sci.* 15:623
27. Gibson LJ, Ashby MR. 1982. *Proc. R. Soc. London Ser. A* 382:43
28. Warren WE, Kraynik AM. 1988. *J. Appl. Mech.* 55:341–46
29. Kraynik AM, Neilsen MK, Reinelt DA, Warren WE. 1999. In *Foams and Emulsions*, ed. JF Sadoc, N Rivier. Netherlands: Kluwer
30. Zhu HX, Knott JF, Mills NJ. 1997. *J. Mech. Phys. Solids* 45(3):319
31. Gent AN, Thomas AG. 1959. *J. Appl. Poly. Sci.* 1:7
32. Matonis VA. 1964. *Soc. Plast. Eng. J.* (Sept.) p. 1024
33. Chan R, Nakamura M. 1969. *J. Cell. Plast.* 5:112
34. Barma P, Rhodes MB, Salover R. 1978. *J. Appl. Phys.* 49:4985
35. Christensen RM. 1986. *J. Mech. Phys. Solids* 34:563–78
36. Zhu HX, Mills NJ, Knott JF. 1997. *J. Mech. Phys. Solids* 45 (11–12):1875–904
37. Mills NJ, Zhu HX. 1999. *J. Mech. Phys. Solids*. 47(3):669–95
38. Warren WE, Kraynik AM. 1997. *J. Appl. Mech.* 64:787–94
39. Simone AE, Gibson LJ. 1998. *Acta Mater.* 46:2139–50
40. Grenestedt JL. 1998. *J. Mech. Phys. Solids* 46(1):29–50
41. Hashin Z, Shtrikman S. 1963. *J. Mech. Phys. Solids* 11:127–40
42. Grenestedt JL. 1999. *Int. J. Solids Struct.* 36:1471–501
43. Deshpande VS, Fleck NA. 2000. *J. Mech. Phys. Solids*. In press
44. Bart-Smith H, Bastawros A-F, Mumm DR, Evans AG, Sypeck DJ, Wadley HNG. 1998. *Acta Mater.* 46(10):3583–92
45. Bastawros A-F, Bart-Smith H, Evans AG. 2000. *J. Mech. Phys. Solids* 48:301–22
46. Beals JT, Thompson MS. 1997. *J. Mater. Sci.* 32:3595–600
47. Dubbelday PS. 1992. *J. Acoust. Soc. Am.* 91(3):1737–44
48. Gradinger R, Simancik F, Degischer HP. 1997. *Determination of mechanical properties of foamed metals*. Proc. Int. Conf. Welding Technology, Materials and Materials Testing, Fracture Mechanics and Quality Management. 2:701–22. Vienna: Chytra Druck & Verlag
49. McCullough KYG, Fleck NA, Ashby MR. 1999. *Acta Mater.* 47(8):2323–30
50. Weber M, Baumeister J, Banhart J, Kunze H-D. 1994. *Powder metallurgy*. Conf. Proc. Porosity, Porous Materials. pp. 585–88
51. Andrews EW, Gioux G, Onck P, Gibson LJ. 2000. *Int. J. Mech. Sci.* Submitted
52. Dubbelday PS, Rittenmyer KM. 1985. *Shear modulus determination of foamed aluminum and elastomers*. Proc. IEEE Ultrasonics Symp. 2:1052–55
53. Banhart J, Baumeister J, Weber M. 1995. *Light alloys*. Proc. Euro PM '95. pp. 201–8
54. Banhart J, Baumeister J. 1998. *J. Mat. Sci.* 33(6):1431–40

55. Gioux G, McCormack TM, Gibson LJ. 2000. *Int. J. Mech. Sci.* In press
56. von Hagen H, Bleck W. 1998. *Compressive, tensile, and shear testing of melt-foamed aluminium. Proc. Mater. Res. Soc. Symp.* Proc. Mater. Res. Soc. Symp. 521:59–64
57. Prakash O, Sang H, Embury JD. 1995. *Mater. Sci. Eng. A* 199:195–203
58. Thornton PH, Magee CL. 1975. *Metall. Trans. A* 6A:1253–63
59. Triantafillou TC, Zhang J, Shercliff TL, Gibson LJ, Ashby MF. 1989. *Int. J. Mech. Sci.* 31:665–78
60. Davis JR. 1993. *ASM Specialty Handbook. Aluminum and Aluminum Alloys*, Materials Park, OH: Am. Soc. Met.
61. Simone AE, Gibson LJ. 1998. *Acta Mater.* 46(11):3929–35
62. Grenstedt JL, Tanaka K. 1999. *Scripta Mater.* 40(1):71–77
63. Chen C, Lu TJ, Fleck NA. 1999. *J. Mech. Phys. Solids* 47:2235–72
64. Onck P, Andrews EA, Gibson LJ. 2000. *Int. J. Mech. Sci.* Submitted
65. Gibson LJ, Ashby MF, Zhang J, Triantafillou TC. 1989. *Int. J. Mech. Sci.* 31:635–63
66. Miller RE. 2000. *Int. J. Mech. Sci.* In press
67. Zhang J, Lin Z, Wong A, Kikuchi N, Li VC, et al. 1997. *J. Eng. Mater. Technol.* 119:284–91
68. Andrews EW, Gibson LJ, Ashby MF. 1999. *Acta Mater.* 47:2853–63
69. Finnie I, Heller WR. 1959. *Creep of Engineering Materials*. New York: McGraw Hill
70. Andrews EW, Huang J-S, Gibson LJ. 1999. *Acta Mater.* 47:2927–35
71. Sugimura Y, Rabiei A, Evans A, Harte A-M, Fleck NA. 1999. *Mater. Sci. Eng. A* 269:38–48
72. Harte A-M, Fleck NA, Ashby MF. 1999. *Acta Mater.* 47(8):2511–24
73. McCullough KYG, Fleck NA, Ashby MF. 2000. *Fatigue Fract. Eng. Mater. Struct.* Submitted



CONTENTS

The Theory of Real Materials, <i>Marvin L. Cohen</i>	1
Tribochemical Polishing, <i>Viktor A. Muratov, Traugott E. Fischer</i>	27
High-Tc Superconductivity in Electron-Doped Layered Nitrides, <i>Shoji Yamanaka</i>	53
Holographic Polymer-Dispersed Liquid Crystals (H-PDLCs), <i>T. J. Bunning, L. V. Natarajan, V. P. Tondiglia, R. L. Sutherland</i>	83
Optical Generation and Characterization of Acoustic Waves in Thin Films: Fundamentals and Applications, <i>John A. Rogers, Alex A. Maznev, Matthew J. Banet, Keith A. Nelson</i>	117
Structure Evolution During Processing of Polycrystalline Films, <i>C. V. Thompson</i>	159
Mechanical Behavior of Metallic Foams, <i>L. J. Gibson</i>	191
Copper Metallization for High-Performance Silicon Technology, <i>R. Rosenberg, D. C. Edelstein, C.-K. Hu, K. P. Rodbell</i>	229
The Properties of Ferroelectric Films at Small Dimensions, <i>T. M. Shaw, S. Trolier-McKinstry, P. C. McIntyre</i>	263
IC-Compatible Polysilicon Surface Micromachining, <i>J. J. Sniegowski, M. P. de Boer</i>	299
SiGe Technology: Heteroepitaxy and High-Speed Microelectronics, <i>P. M. Mooney, J. O. Chu</i>	335
Ultrathin Diffusion Barriers/Liners for Gigascale Copper Metallization, <i>A. E. Kaloyeros, E. Eisenbraun</i>	363
Magnetocaloric Materials, <i>K. A. Gschneidner Jr., V. K. Pecharsky</i>	387
Advances in In Situ Ultra-High Vacuum Electron Microscopy: Growth of SiGe on Si, <i>Ruud M. Tromp, Frances M. Ross</i>	431
Layered Magnetic Manganites, <i>T. Kimura, Y. Tokura</i>	451
The Electronic Structure of Semiconductor Nanocrystals, <i>Al. L. Efros, M. Rosen</i>	475
Mechanisms for Enhanced Formation of the C45 Phase of Titanium Silicide Ultra-Large-Scale Integration Contacts, <i>J. M. E. Harper, C. Cabral Jr., C. Lavoie</i>	523
Synthesis and Characterization of Monodisperse Nanocrystals and Close-Packed Nanocrystal Assemblies, <i>C. B. Murray, C. R. Kagan, M. G. Bawendi</i>	545
Extremely High Density Longitudinal Magnetic Recording Media, <i>Dieter Weller, Mary F. Doerner</i>	611
Low Dielectric Constant Materials for ULSI Interconnects, <i>Michael Morgen, E. Todd Ryan, Jie-Hua Zhao, Chuan Hu, Taiheui Cho, Paul S. Ho</i>	645
Device Innovation and Material Challenges at the Limits of CMOS Technology, <i>P. M. Solomon</i>	681